Computational Icing Analysis on NASA's SIDRM Geometry to Investigate Collection Efficiency

Eric A. Stewart
Naval Air Warfare Center Aircraft Division, Patuxent River, MD, 20670, USA

Tadas P. Bartkus
Ohio Aerospace Institute, Cleveland, OH, 44142, USA

Abstract

Computational icing analysis results were compared to experimental icing tunnel data including aerothermal (e.g., dry air) and supercooled water droplet rime-ice conditions from tests conducted in early 2022 at the NASA Icing Research Tunnel (IRT). The Simulated Inter-compressor Duct Research Model (SIDRM) test article was used in this study, and its geometry represents the inter-compressor duct region of a turbofan engine. The test article's purpose is to study the physics of supercooled water icing and ice crystal icing. This study compared three different icing codes: FENSAP-ICE (Eulerian approach), LEWICE3D (Lagrangian approach), and GlennICE (Lagrangian approach). All three icing codes were conducted on SIDRM's complex body flow-field and compared to different experimental supercooled water rime runs. The test article instrumentation (pressure taps, thermocouples, etc.) and 3D laser scans of final ice shapes were used to compare against the different icing code simulations. The overall objectives are to understand how the icing codes handle capturing collection efficiency on the complex test article's unheated surfaces. In the aerothermal cases, pressure tap readings matched the CFD results, but dry air CFD underpredicted thermocouple readings. Collection efficiency results from all three icing codes matched well together on the main body leading edge, main body slope, and the strut leading edges. Rime experimental collection efficiency was calculated from the raw 3D laser scan of the ice shape using a traditional equation. Results showed different matches to the icing codes at the main body nose, ramp, and strut leading edges. All three icing codes underpredicted the final ice shape using a single-shot constant ice density approach, with more difficulty coming from the strut leading edge ice shape due to the swept wing like flow field. NASA's overall goal for this effort is to develop computational icing tools to assist in the design and certification of engines for flight in icing conditions.

Introduction

Aircraft engine ice crystal ingestion is a growing concern that can be attributed to many engine power-loss events with possible failure modes of engine stall, rollback, flameout, and physical damage to the compressor blades [1]. Ice crystals ingested into the turbofan engine will deflect and break-apart coming off the fan stage. The portion of ice crystals that enter the lower stages of the compressor will face warmer than freezing temperature gradients that will melt the ice-crystal and generate a mixed-phase condition. The ice-crystals will eventually impact compressor shroud wall surfaces and form a thin water film layer at the wall surface. Additional ice-crystals impacting the same wall will stick to the water film layer and begin to lower the wall temperature through convection and evaporative cooling. Over time, the wall surface temperature can decrease enough for ice to adhere between the wall and water film surface. Ice will continue to accumulate until aerodynamic forces cause the ice to break from the surface and shed off the surface [1]. Previous studies in 2018 were conducted with a NACA 0012 airfoil test article by NASA Glenn Research Center in their 2nd Fundamental Ice Crystal Icing Physics Test at NASA Glenn's Propulsion Systems Laboratory to better understand ice crystal icing (ICI) [2-4].

The Simulated Inter-compressor Duct Research Model (SIDRM) test article represents the inter compressor duct region of a turbofan engine. Figure 1 shows the outer shroud wall's complex geometry inside the inter compressor duct with inlet guide vane "struts". The SIDRM test article represents this axisymmetric wall by use of a 2D extruded wall polynomial shape with a single strut junction at the centerline of the test article's 1.82 m (~6 ft) span. The struts on SIDRM are NACA0012 at 0° AoA with 101.6 mm (4 in) chords. SIDRM is a symmetric geometry about its centerline. The test article has heated zones on the main section that can be controlled independently, and the test article is instrumented with heat flux gauges, thermocouples, and pressure taps. The ability for the test article to heat its outer-mold-line (OML) surfaces is necessary when trying to simulate the warm inner surfaces of the turbofan inter compressor duct region. SIDRM went through a series of icing physics tests in the Icing Research Tunnel (IRT) targeted at producing icing code development data [5-6]. With well-characterized icing conditions these past tests will help in developing future computational icing models to study ice crystal and supercooled water droplet accretion on a complex sloped wall surface and at a strut junction with that wall.

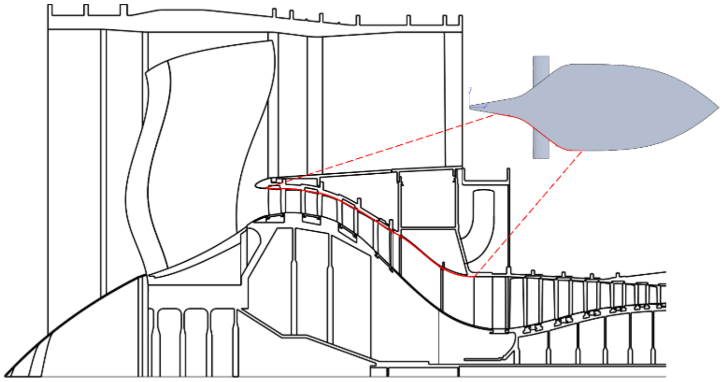

Figure 1. How SIDRM's test article geometry relates to a turbofan's inter-compressor duct outer shroud wall [7].

In addition to targeting ice crystal tunnel runs, super cooled liquid water droplet runs were conducted. Supercooled liquid icing tests provide a baseline for icing code simulation validation data on the new 3D geometry. One of the more difficult validation data to collect is collection efficiency. Collection efficiency is the fraction of water mass flux accumulated on a point of the test article surface compared to the upstream freestream droplet water mass flux [8]. The impingement or collection efficiency, β, will be higher for super cooled liquid water droplets compared to ice crystals due to ice crystals having the ability to bounce off the surface if they cannot stick to a water film surface layer. More information on the SIDRM test article, the icing tests, and the icing cloud characterization tests can be found in Bartkus et al. [5].

This paper will cover an icing study analyzing different icing codes involving FENSAP-ICE (Eulerian approach) [9], LEWICE3D (Lagrangian approach) [10], and GlennICE (Lagrangian approach) [11] on SIDRM's complex body flow-field and be compared to experimental icing tunnel rime runs. The test article instrumentation and 3D laser scans of the final ice shapes in the run will be used to validate and compare the icing code simulations. This paper is in conjunction with a paper by Bartkus et al. [12] that provides supercooled liquid icing results from the SIDRM icing tests in 2022.

Experimental Data Analysis

A depiction of the SIDRM test article mounted on the turn table inside the IRT tunnel test section can be seen in Fig. 2. For more information on the experiment setup and measurement instrumentation see Bartkus et al. [5].

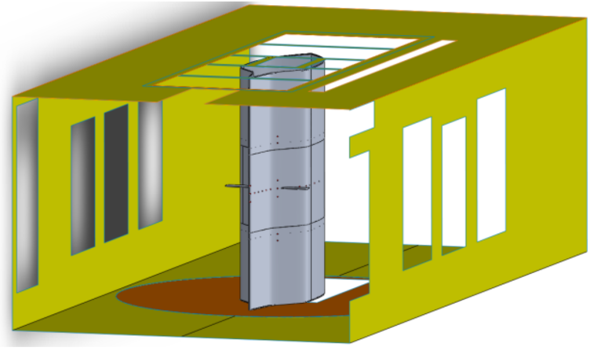

Figure 2. SIDRM test article setup inside the NASA IRT's test section.

Experimental Setup

For aerodynamic characterization, SIDRM has a total of 64 pressure taps that are split between an upper and lower row on the test article. Figure 3 shows a 2D side view of the nominal locations of the upper and lower pressure tap rows (labeled as Pxxx) on what is referred to as the "instrumented side". Pressure taps are on both the upper surface and lower surface sides of the test article, and some are placed staggard at the leading-edge (LE) nose shown in Fig. 4. Note the vertical line seen near the coordinate system is not at the exact leading edge of the main body and is only the intersection of the surface panels. Also note this global coordinate system is different than the coordinate system presented in Bartkus et al. [12] due to the needs of the icing codes. Thermocouple's T201, T301, and T401 are located at the leading edge. Figure 3 shows the thermocouples (labeled as Txxx and STx) on the instrumented side. There are also five additional thermocouples on the other side or "non-instrumented side," and they are referred to as the "back side" thermocouples in this paper.

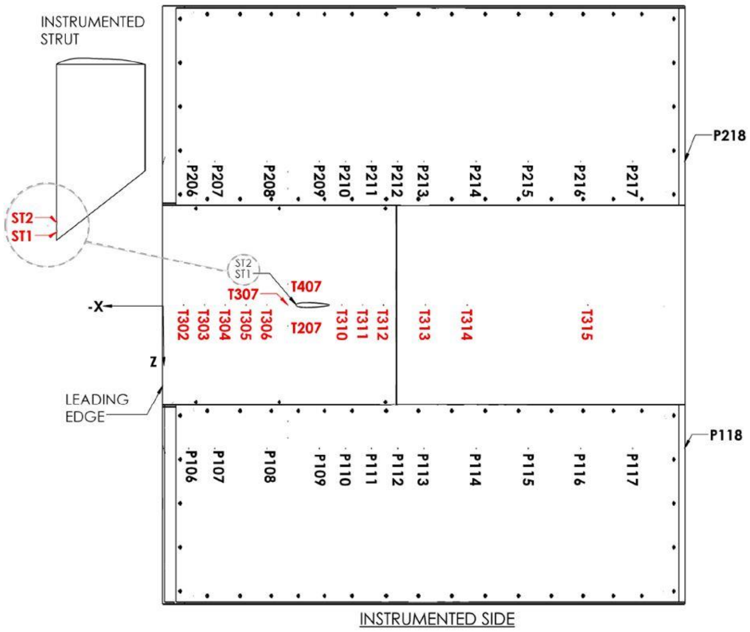

Figure 3. Pressure tap (Pxxx) and thermocouple (Txxx and STx) locations on SIDRM's instrumented side.

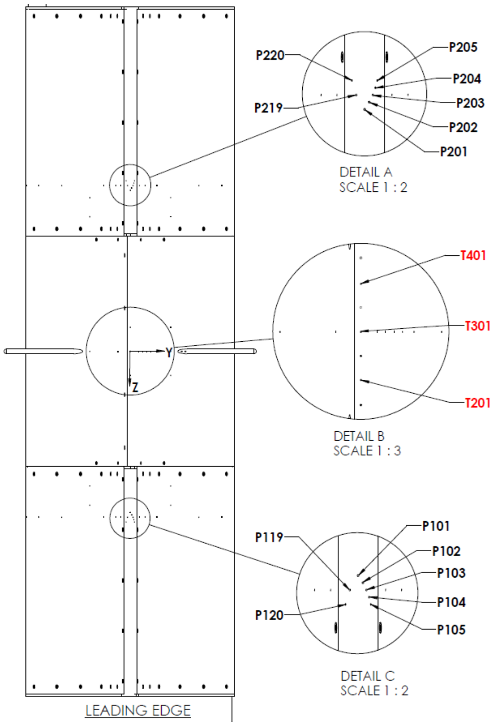

Figure 4. View of pressure tap and thermocouple locations on SIDRM's leading edge.

During the aerothermal runs, the test article was swept through angle of attack changes (0, 1, 2, 3, and 4°) and tunnel airspeed changes of 50, 100, 150, 200, and 230 knots. Total temperature was targeted to remain constant during the airspeed sweep, but this ended up varying due to various limitations and testing time.

Simulated Dry Air Aerothermal Validation Cases

The computational icing code process for FENSAP-ICE, LEWICE3D, and GlennICE requires calculating the "dry air" (no icing cloud and no humidity) Navier-Stokes flow solution and inputting that into each icing code. The dry air computational fluid dynamics (CFD) simulations were conducted, and they were compared to the pressure tap and thermocouple measurements in SIDRM's aerothermal runs. An aerothermal run is different than an icing run in the IRT, with the main difference being that no icing cloud is produced by the spray bars during the run. Aerothermal runs are preferred for validation because during an icing run all pressure taps are provided positive pressure to prevent icing within the pressure taps. Table 1 lists the aerothermal runs that were chosen for validation.

Table 1. Aerothermal Cases Used in Validation Study

Test Date	Cobra Test ID (#)	Tunnel T_{total} (^{O}C)	Air Speed (Knots)	Tunnel P_{static} (Pa)	AoA (Deg)
2/16/2022	3	5.23	150.3	95626.7	0
2/16/2022	10	5.43	200.1	92854.9	0
2/16/2022	12	5.26	230.2	90825.7	0
4/11/2022	12	3.73	150.5	94654.8	4

The SIDRM test article geometry, including the NACA0012 101.6 mm (4 inch) chord struts, was meshed inside the IRT's rectangular tunnel test section. SIDRM's high flow blockage causes the preference of a rectangular prism tunnel grid over a spherical far-field grid due to constrained air flow between the test article and tunnel walls. The inlet and outlet of the IRT tunnel was extended about 12 body lengths from the test article to ensure convergence stability and to not rely as much on the pressure outlet value behind SIDRM. Angle of attack changes were created by rotating the test article and wake planes and re-generating a new volume mesh. The mesh was composed of using a hybrid mesh of prism layers (with y+ ~1 at the fastest tunnel speed) at the surface and an unstructured tetrahedral for the rest of the volume grid. Grid refinement was placed around the test article and downstream to capture the wake. The mesh for the 0° AoA can be seen in Fig. 5 and shows the tunnel geometry and refined mesh around the test article. Total mesh is around 13.8 million cells.

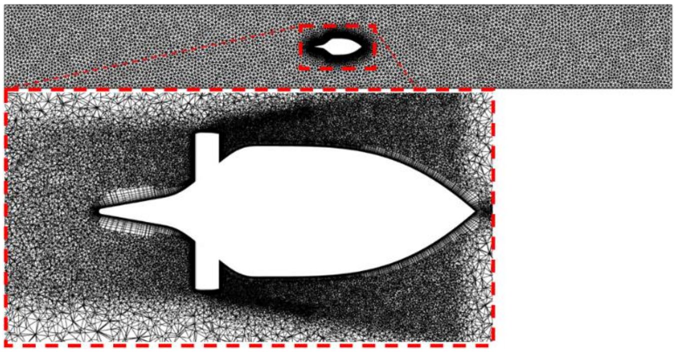

Figure 5. Tunnel grid mesh and refined mesh around the SIDRM test article.

Dry air CFD simulations were run in ANSYS Fluent [13] using the Spalart-Allmaras Turbulence model with viscous heating and curvature correction enabled. The viscous heating option was activated for the viscous dissipation terms and to better simulate the thermal energy generated by the fluid viscous shear at the wall [13]. This viscous heating option was selected because turbulent heat fluxes are needed to capture the ice accretion. A velocity inlet and pressure outlet boundary condition were applied to the tunnel grid, and a no-slip surface and fixed surface temperature on the test article. FENSAP-ICE requires a wall thermal boundary condition of around Total Temp+10°K wall surface temperature, while GlennICE requires two flow solutions with different thermal wall temperatures at the surface to calculate the true adiabatic wall surface temperature inside the icing code. The tunnel walls were simulated with an inviscid boundary condition due to the assumption that the boundary layer effects on the test article centerline icing cloud and pressure tap row measurements are negligible. Static pressures and total temperatures in the simulations matched the IRT tunnel measurements during the runs. Aerothermal runs were recorded for 30 sec after the tunnel reaches equilibrium and an average of that 30 sec was used as the boundary condition input values. SIDRM's separation near the trailing edge required running a few thousand iterations until the coefficient of lift and drag plateaued and reached a steady-state convergence.

Figure 6 details the slice locations on the main body analyzed for the CFD results for the aerodynamic pressure comparisons. Note the centerline and x-axis of SIDRM goes through the NACA0012 struts. The maximum thickness of the strut protrudes out to ± 6.096 mm (± 0.24 in) in the z-axis "main body spanwise" direction. Slices taken at ± 19.05 mm (± 0.75 in) were intended to investigate the pressure field change from the strut at the junction between the strut root and main body. Slices taken at 152.4 mm (6 in) and 304.8 mm (12 in) are for investigating areas not affected by the strut and to see how the convergence of the results look spanwise. Figs. 7-9 shows good agreement between dry air CFD predictions (line curves) and all 64 experimental pressure taps (symbols) for tunnel airspeeds of 150, 200, and 230 knots with the test article at 0° angle of attack (AoA). In addition, Fig. 10 for the 150 knots and the test article at 4° showed the simulation matched the pressure tap readings on the pressure and suction sides. For the plots, pressure coefficients are plotted against the normalized chord length (x represents the chordwise direction and c is the chord length). The CFD slice data from the upper and lower surfaces of the main body are laying right on top of each other because the simulation is at 0°. The upper and lower pressure tap rows are identified by different symbols. For Figs. 7-9 at 0° AoA, they should overlap with each other, but some locations are off in the non-separated flow regions. The simulation predicts flow separation, where the Cp flattens to the trailing edge, at x/c = 0.82, and these variances in slice locations show the simulation having difficulty converging the separation location in these steady-state simulations.

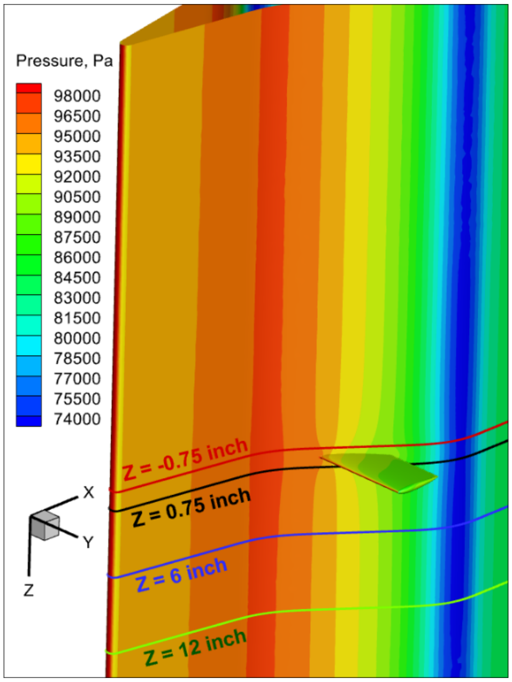

Figure 6. Dry air CFD pressure contour in Pa units with slice locations shown for 200 knots and 0° AoA case.

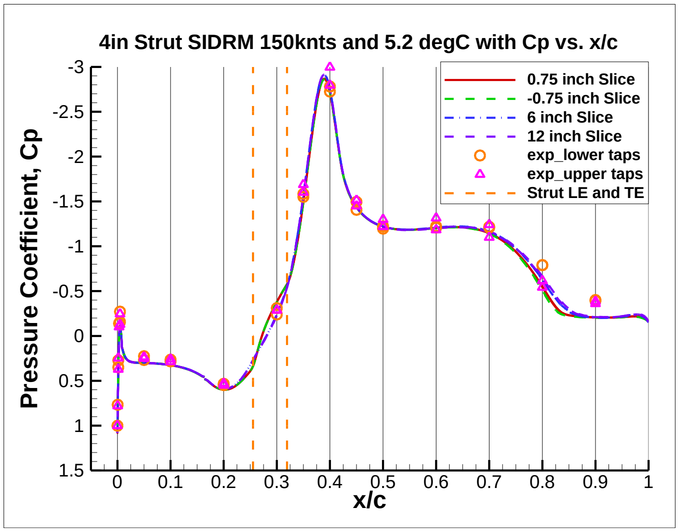

Figure 7. Dry air CFD to experimental Cp vs. x/c comparison at 150 knots and 0° AoA.

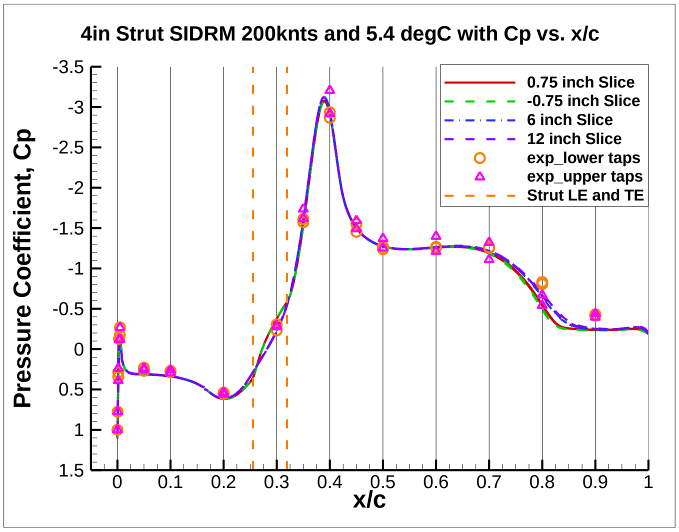

Figure 8. Dry air CFD to experimental Cp vs. x/c comparison at 200 knots and 0° AoA.

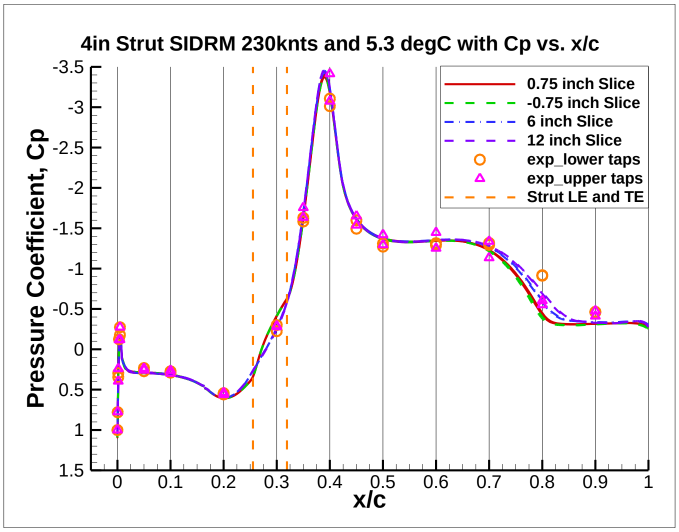

Figure 9. Dry air CFD to experimental Cp vs. x/c comparison at 230 knots and 0° AoA.

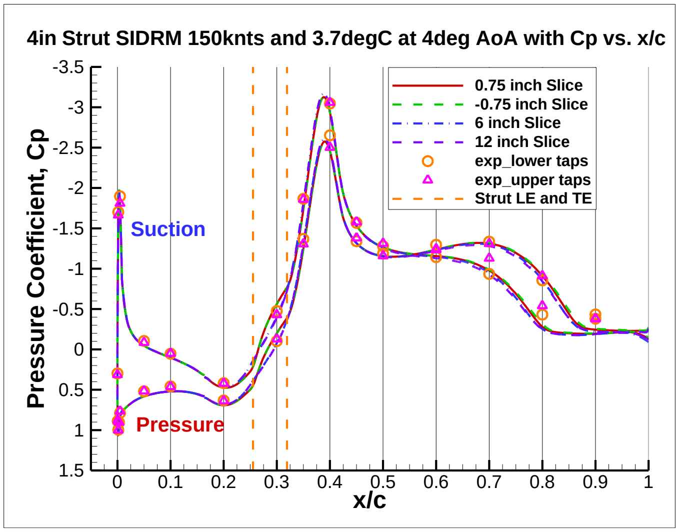

Figure 10. Dry air CFD to experimental Cp vs. x/c comparison at 150 knots and 4° AoA.

To get the dry air CFD surface temperature, another CFD simulation is needed where the test article wall boundary condition is changed from a fixed wall temperature to a zero-heat flux condition. ANSYS Fluent calculates what the adiabatic wall temperature should be, and that result is used to compare to the experimental thermocouple measurements. Figures 11-13 shows the trend between the prediction and measurements to be in agreement between CFD predictions (line curves) and all 20 main body experimental thermocouples (symbols) for tunnel airspeeds of 150, 200, and 230 knots with the test article at 0° angle of attack (AoA). Temperature differences can be from the test article not reaching equilibrium in the aerothermal run and from the tolerance of the thermocouples themselves. In addition, the thermocouples were imbedded flush with the surface, and they are likely measuring warmer temperatures due to being closer to the heaters on the inner-mold-line side. The 4° AoA case shown in Fig. 14 shows a ± 0.5°K agreement with the instrumented side and back side thermocouples to the CFD.

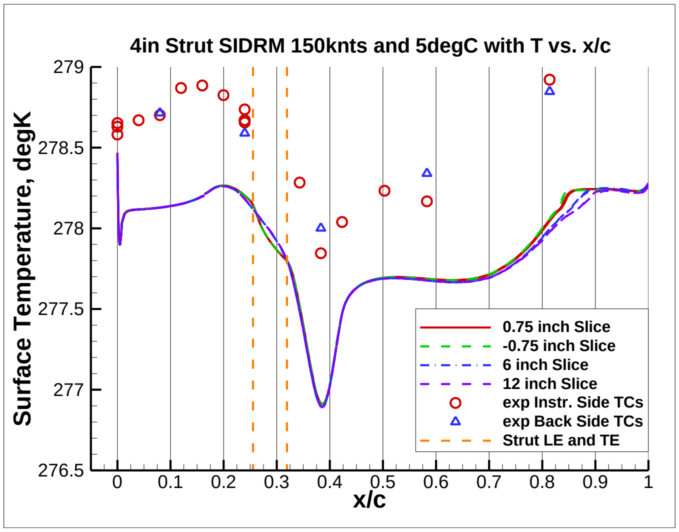

Figure 11. Dry air CFD to experimental surface temp comparison at 150 knots and 0° AoA.

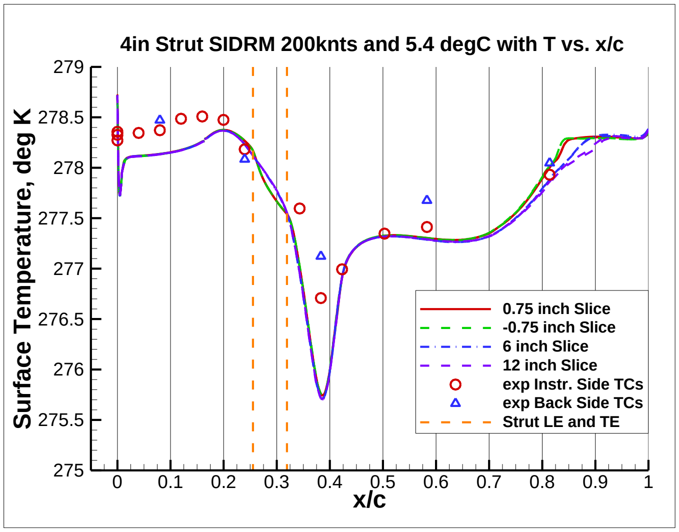

Figure 12. Dry air CFD to experimental surface temp comparison at 200 knots and 0° AoA.

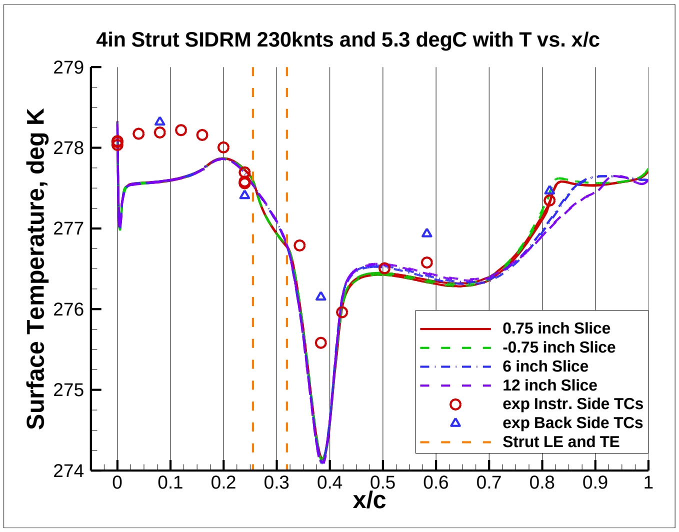

Figure 13. Dry air CFD to experimental surface temp comparison at 230 knots and 0° AoA.

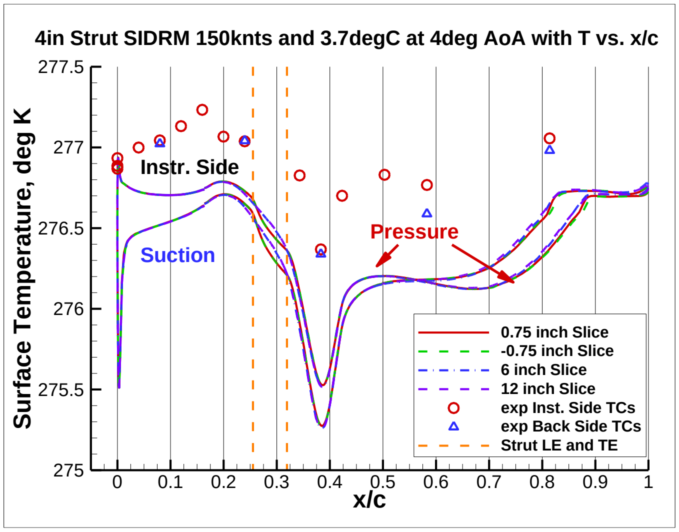

Figure 14. Dry air CFD to experimental surface temp comparison at 150 knots and 4° AoA.

Icing Code Methodology

The icing codes used the same dry air flow solutions from the ANSYS Fluent run as inputs. Collection efficiency and ice shapes for supercooled liquid water droplets were calculated for SIDRM's geometry using FENSAP-ICE, LEWICE3D, and GlennICE.

The ANSYS FENSAP-ICE v2021 R1 code uses a Eulerian approach for droplets and for solving the heat and mass balance for the control volume. FENSAP-ICE's DROP3D and ICE3D in sequence were the main modules used in this analysis with this icing code. DROP3D is a 3D finite element Eulerian water droplet/ice crystal impingement solver that was used to simulate different cloud droplet/ice-crystal distributions. ICE3D takes the data from DROP3D and uses a 3D finite volume water runback and ice accretion solver. It can produce water film thickness, 3D ice accretion shapes, and final surface temperatures [9]. For collection efficiency it is defined as,

$$\boldsymbol{\beta} = -\frac{\boldsymbol{LWC_{local}\vec{V}_d \cdot \vec{n}}}{\boldsymbol{(LWC_\infty)V_\infty}} \qquad \text{Eq-1}$$

where is the $\vec{V}_d$ droplet velocity vector, V_∞ is freestream velocity, and $\vec{n}$ is the surface normal vector. Liquid water content (LWC) local and freestream are designated with LWC_{local} and LWC_∞. To calculate the ice accretion and water runback, ICE3D uses a thin-film Shallow-Water Icing Model (SWIM), which is a thermodynamic model based on a system of partial differential equations [14]. The SWIM uses the convection heat transfer to define the cooling effect and shear stress from the flow solver to calculate the runback from the airflow solution as an input, rather than using an empirical equation. Heat transfer coefficient is derived by the CFD turbulence model. FENSAP-ICE utilizes native Fluent exports and does not need any processing to read in the dry air solution. The guideline for default droplet convergence used is 1e-10 for residual change in total beta (β), but some smaller size droplet runs oscillated in the 1e-07 range for these SIDRM simulations.

The LEWICE icing software was developed by the Icing Branch at the NASA Glenn Research Center for the analysis of the ice accretion process on airframes, and the code uses a Lagrangian approach for tracking individual stream tubes representing a small finite area and an inviscid potential flow calculation. LEWICE3D v3.6.3 was developed for 3D complex flows and can utilize the flow solutions from other CFD solver programs, but the software uses a two-dimensional cut approach using the two-dimensional LEWICE software for calculating the ice growth at the interest area. A Monte-Carlo approach is used for water droplet stream tubes. Here collection efficiency is calculated as the freestream area of the impinging upstream stream tubes divided by the area of the surface cell impacted. LEWICE3D uses a single time step approach to calculating the ice profile shape. The software calculates the thermodynamics of the freezing process of super-cooled droplet impingement to evaluate the effects of various icing conditions [10]. The Fluent dry air solution was imported into Tecplot, and all needed variables were converted from cell centered to node centered. Then Tecplot was outputted as a .szplt file. A Tecplot to LEWICE3D converter was used to nondimensionalize the variables and put them into a format that LEWICE3D's Trajgrid could read. A constant ice density, RHOI variable name, was set for most of the analysis, but a swept wing ice density model, IDENSITYM=1, was used for one case as an additional comparison. This model calculates the ice density for swept wing flows based off correlations to experimental data with curvature correction factors [15].

The newer GlennICE (Glenn Icing Computational Environment) v2.2 icing software also uses a Lagrangian approach but utilizes a newer adaptive refinement algorithm tracking method [15-17] designed for 3D viscous flow solutions. It can utilize the discretized flow field generated from the CFD flow solvers. GlennICE mainly requires pressure, density, (u, v, w) velocity components, and (x, y, z) surface wall shear component variables. For the ANSYS Fluent solutions, GlennICE needs an insert variable of Cell Wall Distance that is used in the adaptive refinement algorithm. The heat transfer coefficient or the wall heat flux with the surface temperature are needed for ice grow calculations. In this analysis, temperature (only needs surface temperature), heat transfer coefficient (htc), and surface heat flux were output from Fluent. Ice accretion is solved for the entire 3D surface, and heat transfer coefficient can be provided from the CFD turbulence model or calculated in GlennHT using two constant surface temperature runs [11]. GlennICE has a built in Tecplot to GlennICE converter to read in the .szplt flow solution generated for LEWICE3D. Droplets used the adaptive refinement algorithm targeting a high fraction contained tolerance on the boundary surfaces of interest to ensure convergence. For the ice growth, the McClain roughness model with turbulent htc augmentation of 5.0 and an ideal rime limit of 0.009 were used for the final ice shapes.

Supercooled Liquid Collection Efficiency Analysis

This analysis focuses on supercooled liquid droplet rime icing runs and shows the results for three rime ice tunnel runs. The variables that define an icing condition are the cloud median volumetric diameter (MVD), total air temperature (T_{total}), angle of attack (AoA), liquid water content (LWC), relative humidity, and ice accretion time (t). For all rime icing runs, a T_{total} of around -17°C was targeted. The IRT is close to fully saturated as a recirculating tunnel and the relative humidity can be approximated as 100%. The selected icing runs chosen to run in the icing codes can be seen in Table 2.

Table 2. SIDRM Rime Icing Runs Simulated

Test ID (#)	Accretion Time (min)	Tunnel T_{total} (^{o}C)	Air Speed (Knots)	AoA (Deg)	Tunnel P_{static} (Pa)	MVD (µm)	LWC (g/m^3)
UG3548	7	-17.1	200.2	0	91292.5	30	0.45
UG3538	5	-17.0	149.8	0	94141.2	30	0.45
UG3540	5	-17.0	150.5	4	94104.7	30	0.45

For the IRT particle size distribution (PSD) data (from 2019 Calibration) for 29.9µm MVD had 36-bins [18]. To save computational calculation for the runs, an interpolated 7-bin distribution was calculated from the data. This new droplet distribution can be seen in Fig. 15 as the green points vs. the red current IRT distribution. The cumulative fraction is interpolated from a Langmuir D distribution's percent cumulative LWC weight. Only the weight average needs to sum to 100%. Table 3 contains the droplet distribution information used in the icing codes.

Table 3. Interpolated 7-bin Droplet Distribution

Drop Dia. (µm)	Weight (%)
106.7	5
64.4	10
46.4	20
29.9	30
18.6	20
10.7	10
7.5	5

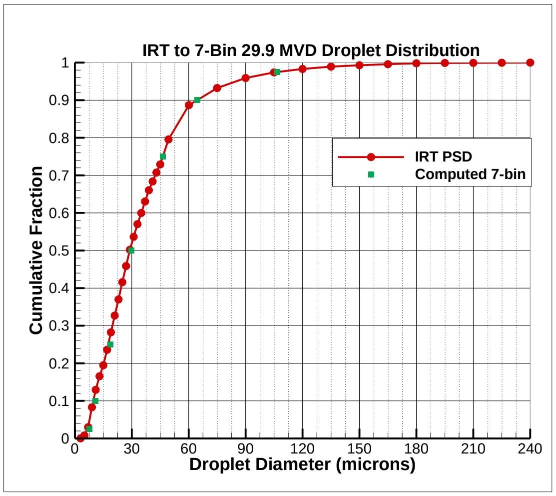

Figure 15. IRT PSD for 29.9µm (2019 Calibration) droplet distribution vs. calculated 7-bin distribution.

An example of collection efficiency for GlennICE for 200 knots at 29.9 µm MVD can be seen in Fig. 16. The slice locations plotted in the following figures can be seen in Fig. 16. Note the STxx thermocouples on the instrumented strut are at about y = 135.6 mm (5.34 in) and y = 145.8 mm (5.74 in).

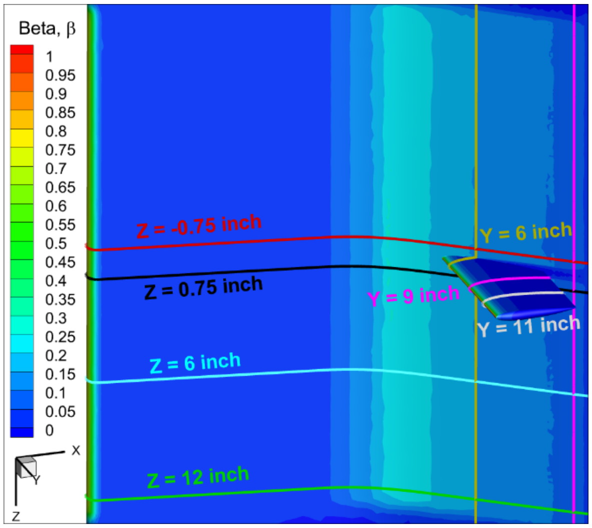

Figure 16. Collection efficiency contour from GlennICE for 200 knots at 29.9µm MVD.

Figures 17-22 show surface air temperature comparison before the spray system is turned on for UG3548 at 200 knots, UG3538 at 150 knots, and UG3540 for 150 knots at 4° AoA. The recorded data before the cloud is around 30 sec. The surface temperature for the z-axis slices on the main body are shown in Figs. 17, 19, and 21 in comparison to the experiment thermocouples. In addition, the surface temperature for the y-axis slices on the instrumented strut are shown in Figs. 18, 20, and 22. The simulation is underpredicting by 1.3°K on the main body and 0.7°K on the strut leading edge. These K-type thermocouples have a tolerance of ±1.1°K for this aerothermal temperature range.

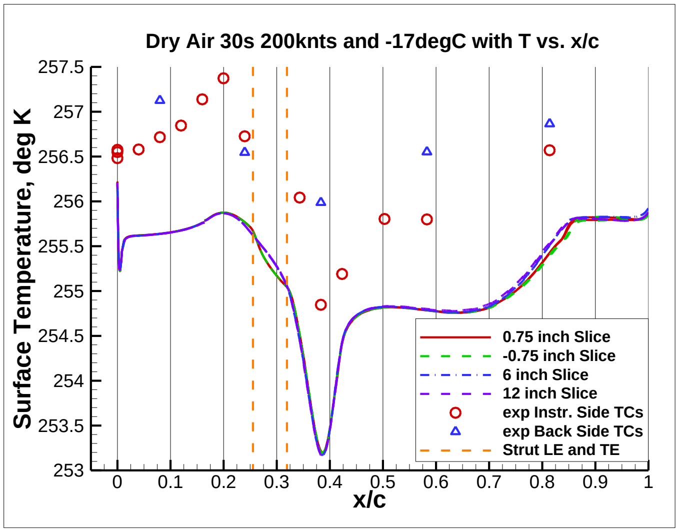

Figure 17. Main body CFD predictions compared to surface temperature measurements for UG3548 at 200 knots and 0° AoA.

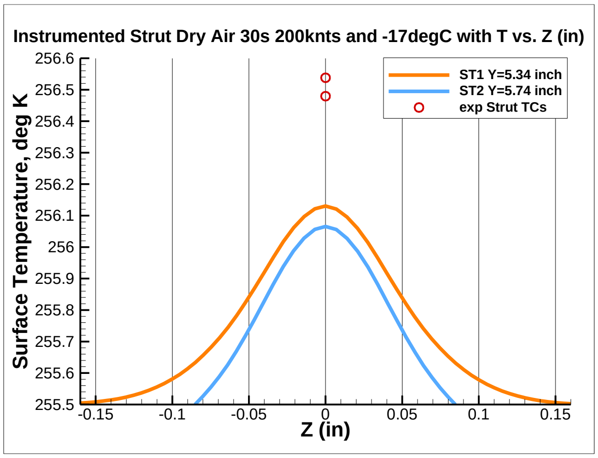

Figure 18. Strut predictions compared to thermocouple measurements for UG3548 at 200 knots and 0° AoA.

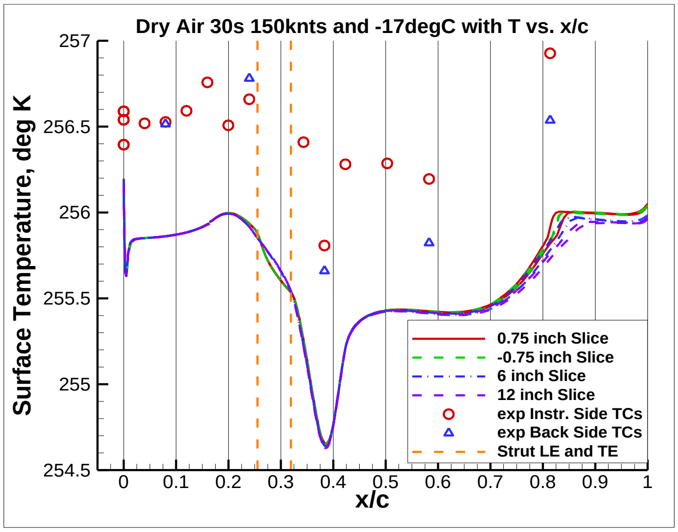

Figure 19. Main body CFD predictions compared to surface temperature measurements for UG3538 at 150 knots and 0° AoA.

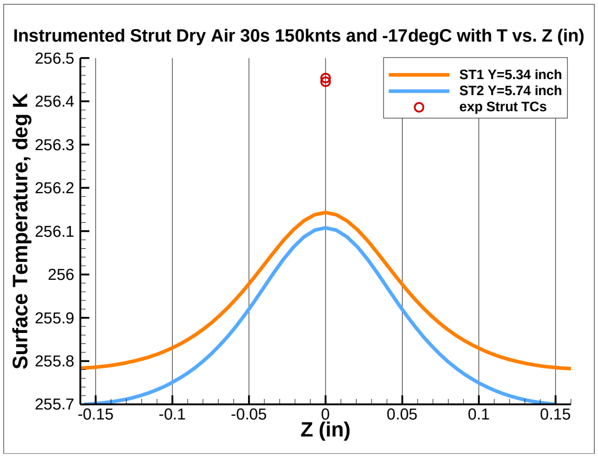

Figure 20. Strut predictions compared to thermocouple measurements for UG3538 at 150 knots and 0° AoA.

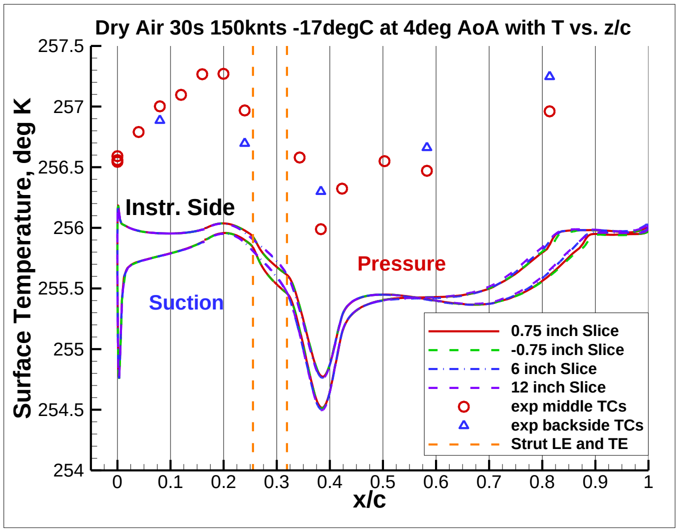

Figure 21. Main body CFD predictions compared to surface temperature measurements for UG3540 at 150 knots and 4° AoA.

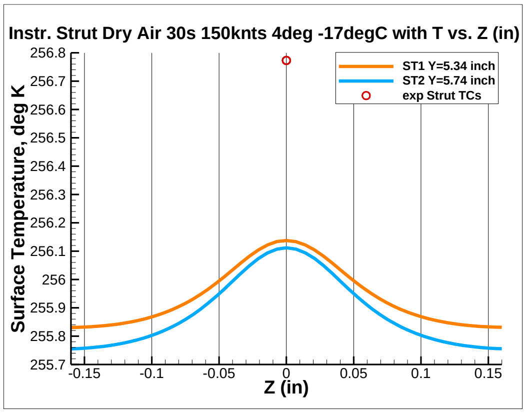

Figure 22. Strut predictions compared to thermocouple measurements for UG3540 at 150 knots and 4° AoA.

Figures 23-25 show the general trends of collection efficiency produced by FENSAP-ICE for UG3548 at 200 knots. Composite curves shown refer to combining and weight averaging 7-bin runs together. Increasing in the positive Y-direction is the same going further outward on the span of the instrumented strut toward the endcap. Collection efficiency increases with increasing y-direction in Fig. 23 on the instrumented strut because local velocity increases further away from the main body surface.

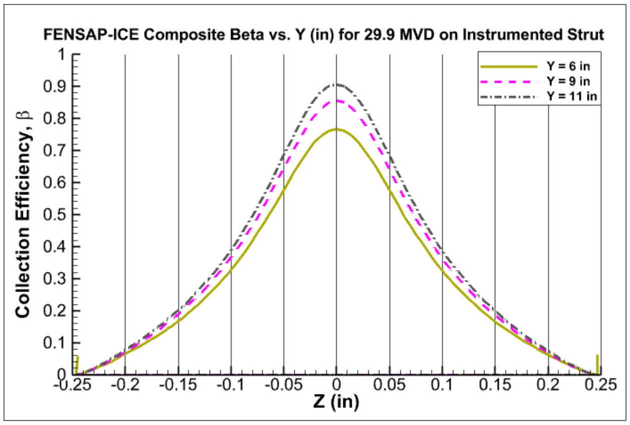

Figure 23. FENSAP-ICE composite beta on the instrumented strut at UG3548 200knts 0° AoA.

To see the trend of changing droplet sizes using FENSAP-ICE, the UG3548 200knts 0° AoA results are plotted in Figs. 24-25 for each bin and the final weight averaged "composite". The beta max peak refers to collection efficiency on SIDRM's leading edge and the smaller peaks "humps" are higher collection efficiency striking on the steep ramp geometry. Increasing droplet size increases collection efficiency at the slope and that secondary beta peak location moves further back on the chord as droplet size increases. For the instrumented strut, Fig. 25 shows increasing droplet size increases beta striking the strut leading edge.

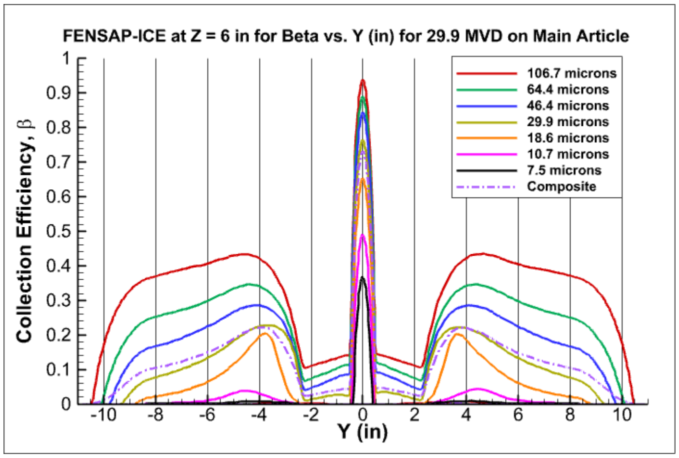

Figure 24. FENSAP-ICE individual droplet bin beta on the main article surface at Z = 6 in for UG3548 200knts 0° AoA.

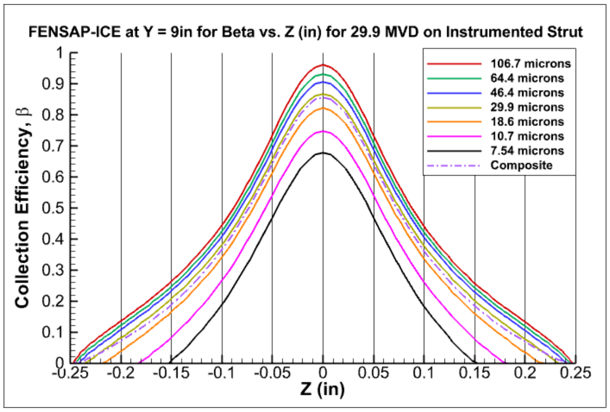

Figure 25. FENSAP-ICE individual droplet bin beta on the instrumented strut leading edge at Y = 9 in slice for UG3548 200knts 0° AoA.

Experimental Collection Efficiency Analysis for 0° AoA

After the rime icing runs, 3D laser scans are taken of the accreted ice shape profile on SIDRM's surface. The final ice profile on the main body and struts were scanned after each icing test run using a 3D laser scanner. The scanned area covered the center +/- 5-inch span, and the scanner has an accuracy range of +/- 0.003". From comparing the 3D laser scans to the clean geometry, ice thickness normal to the surface represented by Δ, can be calculated. For rime cases where freezing fraction $n_0 = 1$ then all the impinging water would freeze on contact with the surface. In these cases, rime ice thickness can be expressed as the following [19]:

$$\Delta = \frac{\boldsymbol{LWC \cdot V \cdot \beta \cdot t}}{\boldsymbol{\rho_{ice}}} \qquad \text{Eq- 2}$$

where liquid water content defined by LWC, freestream velocity by V, collection efficiency by β, and icing duration by t. The ice density will be assumed constant as $\rho_{ice} = 917\, kg/m^3$ unless otherwise stated and is a valid assumption used in all three icing codes for strictly rime simulations. With the experimental rime ice thickness, the collection efficiency can be calculated by rearranging Eq.2.

$$(\boldsymbol{\beta})_{\boldsymbol{exp}} = \frac{\Delta \cdot \boldsymbol{\rho_{ice}}}{\boldsymbol{LWC \cdot V \cdot t}} \qquad \text{Eq- 3}$$

LWC will be assumed as the freestream tunnel constant value. This method for calculating collection efficiency from a rime ice shape has been performed by Tsao and Lee [20] on a swept NACA 0012 wing, and by Tsao and Porter [21] on a Common Research Model Midspan Wing Section model. However, in this test article the upstream leading edge of SIDRM will affect the downstream LWC impacting the sloped wall. This LWC effect can be seen in Fig. 26 from the FENSAP-ICE result where freestream LWC is green and yellow-red represent larger LWC concentration than free stream. A LWC higher concentration is striking the main body ramp and the near the root of the strut.

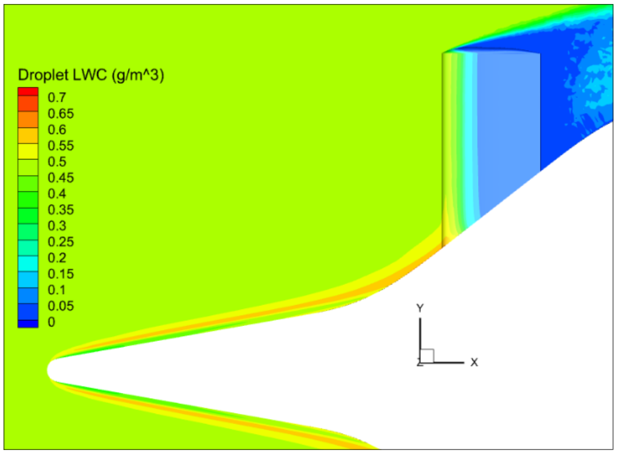

Figure 26. FENSAP-ICE LWC contour at UG3548 200 knots at 0° AoA for the composite to see higher concentration zones.

Even though both V and LWC can vary on the steep ramp slope, a constant freestream method was explored for Eq. 3. In the constant freestream method, a constant freestream tunnel velocity (103 m/s for this UG3548 case) and constant freestream tunnel LWC (0.45 g/m^3 for this case) were used. Figure 27 shows the results for back calculating experimental collection efficiency with a constant $\rho_{ice} = 917\,kg/m^3$ (shown purple) or $\rho_{ice} = 450\,kg/m^3$ (shown orange) compared to the three icing code composite beta results. All three icing codes are on top of each other with only slight differences at the beta peaks. The exp beta curves shows that the main body leading edge collection efficiency is captured well (where beta max is at Y = 0) with $\rho_{ice} = 917\,kg/m^3$, but the slope collection efficiency (strut root LE at Y= ±4.94 in) is not captured when comparing to computational. Switching to $\rho_{ice} = 450\,kg/m^3$ we see that beta max drops significantly, but the slope β is captured better after the peak on the slope. These two ice densities bound what the experimental ice density might be. However, this collection efficiency capture difference could just be due to ice on the main body nose affecting the slope collection efficiency as icing duration time increases.

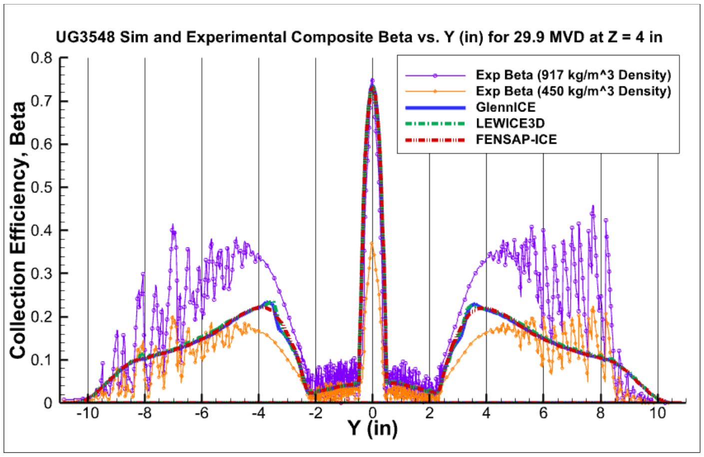

Figure 27. Simulation and experimental beta at the main body slice (Z = 4 in) for UG3548 200 knots rime run.

The same method was applied to an instrumented strut slice at Y = 11 in (279.4 mm). Constant velocity and constant LWC were kept to the tunnel freestream values to not change the definition of collection efficiency. The local velocity is slower than tunnel freestream near the strut leading edge due to the pressure field of the main body. Figure 28 shows the velocity gradient increases going up the instrumented strut from root to tip, and the local flow field behaves more like a swept wing as the air flow is influenced by the main body geometry.

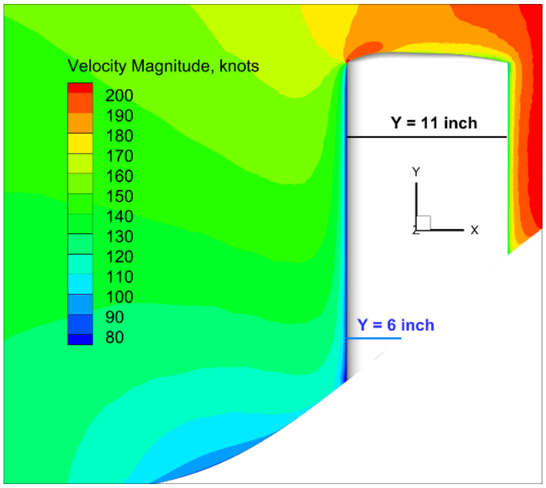

Figure 28. Dry air flow field for UG3538 150 knots at 0° AoA.

Figures 29-30 show using the method used on the experimental ice thickness applied to the strut at a lower slice at Y= 6 in (152.4 mm) and an upper slice at Y = 11 in (279.4 mm). GlennICE and FENSAP-ICE predicted the same collection efficiency results on the strut, but LEWICE3D predicted a lower beta max (Z = 0). Using $\rho_{ice} = 917\,kg/m^3$ for the exp beta created a better match to the icing codes.

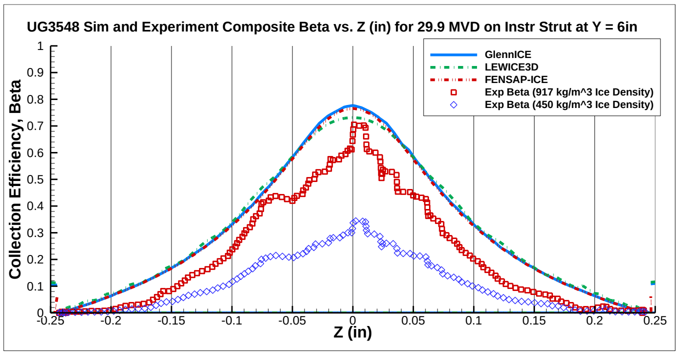

Figure 29. Simulation and experimental beta at the instrumented strut slice Y=6 in for UG3548 200 knots rime run.

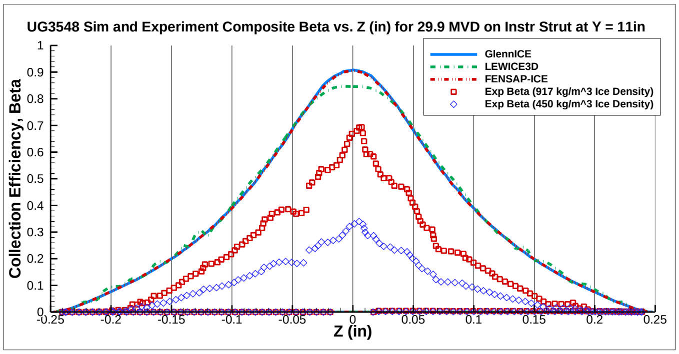

Figure 30. Simulation and experimental beta at the instrumented strut slice Y=11 in for UG3548 200 knots rime run.

Figure 31 shows the results on a lower speed rime icing run at 150 knots, and the trends are identical to the 200 knots case. The oscillating scatter lines in the Exp Beta curves are due to the data being extracted from the raw 3D laser scan data. Where there is oscillation, there are ice feathers on the ramp slope. The base true average slope ice thickness would be in the "valleys" of the ice feather formations. Techniques like maximum combined cross-section (MCCS) could be used to smooth out the feathers in future analysis.

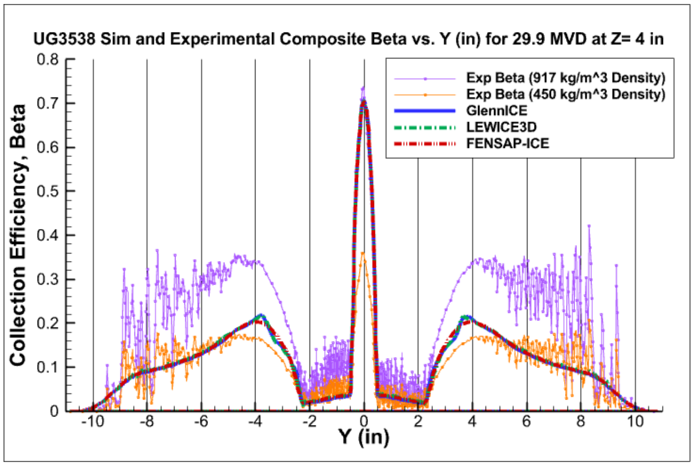

Figure 31. Simulation and experimental beta at the main body slice (Z = 4 in) for UG3538 150 knots rime run.

For the strut slices, the calculated experimental beta in Figs. 32-33, shows the $\rho_{ice} = 917\, kg/m^3$ curve matching to the icing code predictions improves around beta max and the extents for this 150 knots case compared to the 200 knots case. This could just be due to the icing duration for UG3548 200 knots case being 7 mins icing duration vs. the UG3538 150 knots at 5 mins icing duration time. So, a better match due to the smaller ice shape on the test article.

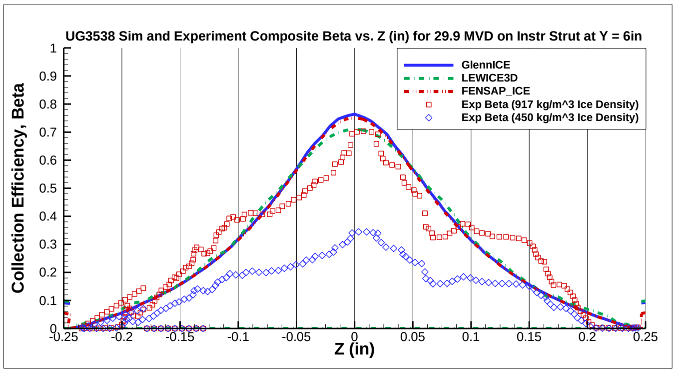

Figure 32. Simulation and experimental beta at the instrumented strut slice Y = 6 in for UG3538 150 knots rime run.

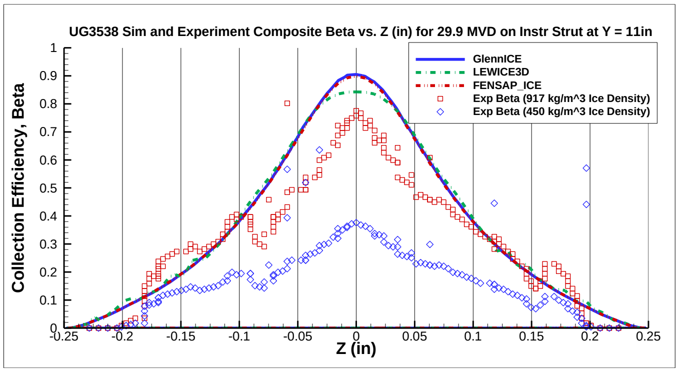

Figure 33. Simulation and experimental beta at the instrumented strut slice Y = 11 in for UG3538 150 knots rime run.

<u>Heat Transfer Coefficient Distribution at 0° AoA and 150 knots</u>

Results for heat transfer coefficient (htc) distribution on the main body can be seen in Fig. 34 for UG3538 150 knots run. GlennICE and FENSAP-ICE have a similar heat transfer coefficient due to both utilizing the data from the CFD solver solution. LEWICE3D uses the Integral Boundary Layer Method for calculating the heat transfer coefficient with modifications for using edge velocity, temperature, and pressure from the volume CFD solution [15]. In Fig. 34, LEWICE3D is calculating a large dip in heat transfer coefficient at the stagnation point on the test article's nose.

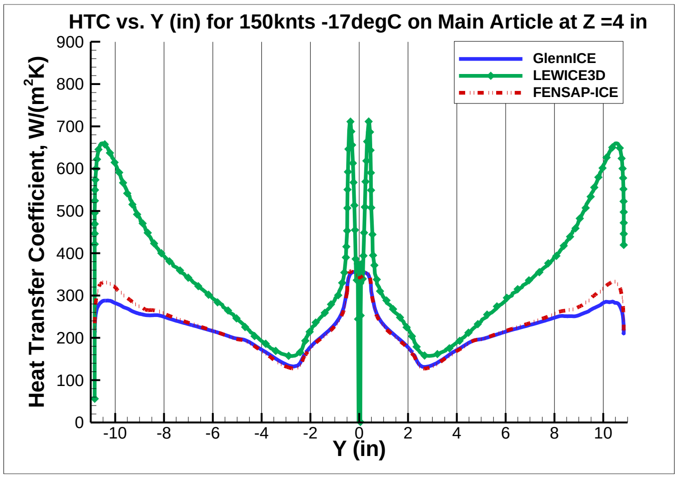

Figure 34. Heat transfer coefficient vs. Y (in) simulation for UG3538 150 knots 0° AoA run at the main body Z = 4 in slice.

Figures 35-36 show the heat transfer coefficient (htc) on the instrument strut slices for the UG3538 150 knots run. Figure 35 (Y= 6 in) shows LEWICE3D calculating a lower htc along the chord, while GlennICE and FENSAP-ICE show a sharper peak formation at the leading edge. The GlennICE, LEWICE3D, and FENSAP-ICE models are using a constant ice density $\rho_{ice} = 917\, kg/m^3$. Figure 36 (Y= 11 in) shows higher max values for heat transfer coefficient than the lower root (Y = 6 in) slice due to the higher velocity at that section cut.

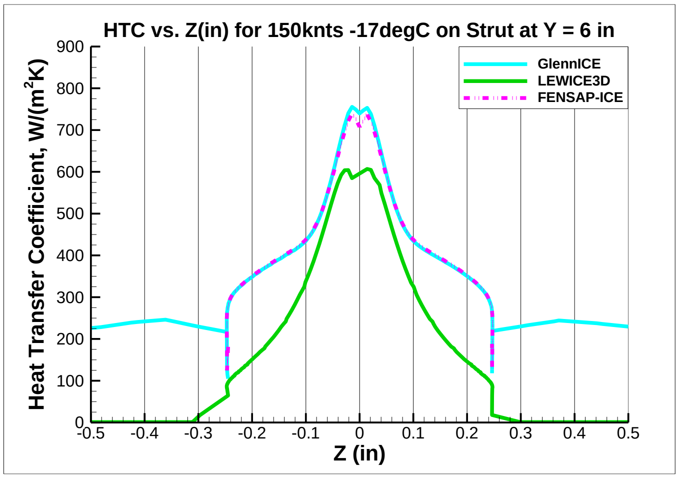

Figure 35. Heat transfer coefficient vs. Z (in) simulation for UG3538 150 knots 0° AoA run at the strut LE lower root Y = 6 in slice.

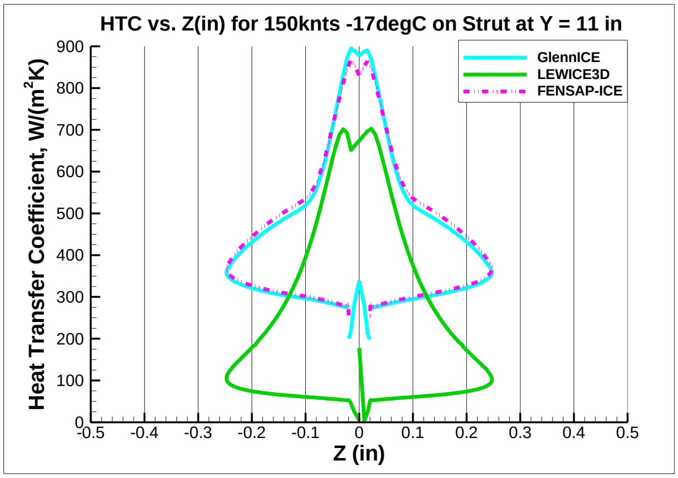

Figure 36. Heat transfer coefficient vs. Z (in) simulation for UG3538 150 knots 0° AoA run at the strut LE upper outboard Y = 11 in slice.

Ice Accretion Analysis at 0° AoA and 200 knots

Results for a single-shot approach and ice density held constant at $\rho_{ice} = 917\, kg/m^3$ are shown in Fig. 37. GlennICE and FENSAP-ICE did not reach the maximum thickness of the experimental ice shapes. LEWICE3D reached the maximum thickness but created a large divot for a rime case. LEWICE3D uses an integral boundary layer method on the 2D slice cut. Perhaps LEWICE3D's edge velocity modification on the small leading edge could be causing the htc calculation to be low enough at the stagnation point to create the large divot shown.

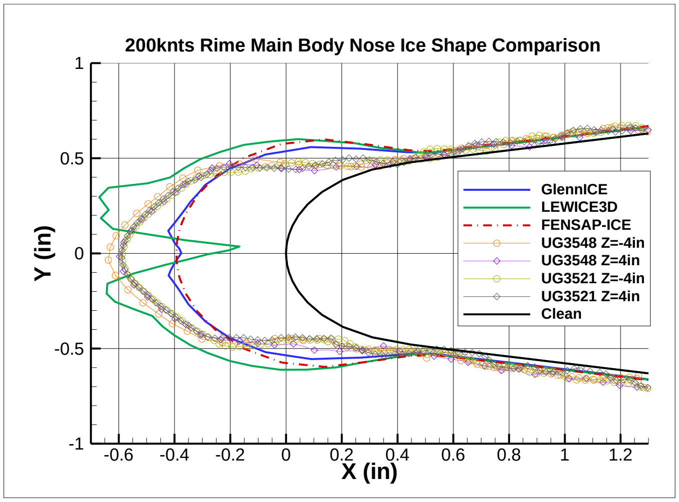

Figure 37. Computational ice shape vs. experimental UG3548 200 knots 0° AoA run at the main body nose for a 7 min icing duration.

Figure 38 shows a centerline line slice focusing on the main body and instrumented strut root junction, where the strut leading edge is shown as a vertical black line. For the slope ice in Fig. 38 all three icing codes produced comparable results at the slope, but LEWICE3D formed thicker ice on the strut. The experimental laser scan results of UG3548 and repeat run of UG3521 are also plotted. The increase in experimental ice thickness might be captured better in a multi-shot simulation approach at this area or a lower ice density. As the nose leading edge ice grows then it will affect droplet trajectories hitting the slope ice.

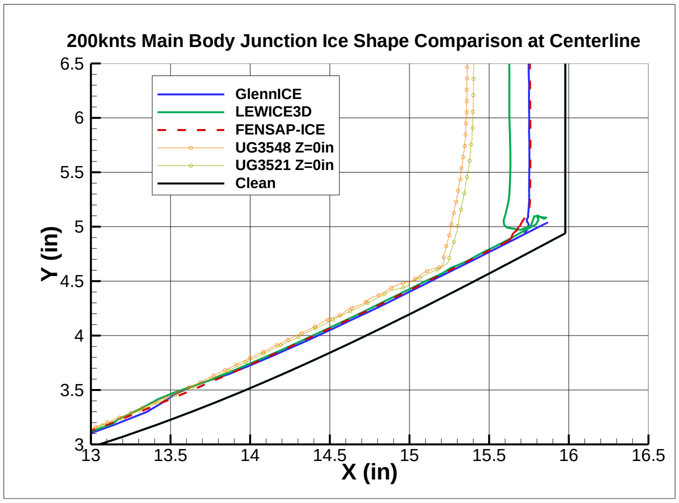

Figure 38. Computational ice shapes vs. experimental UG3548 200 knots 0° AoA run at the main body slope and strut junction for a 7 min icing duration.

Ice comparisons on the instrumented strut can be seen in Figs. 39-40, where LEWICE3D got closer in prediction than GlennICE and FENSAP-ICE to the experimental ice shapes. Since this is a 0° AoA case slices on the non-instrument strut (Y = -6 in and Y = -11 in) are plotted as well for comparison. LEWICE3D overpredicts on Fig. 39 on the lower root slice cut and underpredicts on the Fig. 40 upper outboard slice cut. This seems to be due to LEWICE3D relying on a 2D slice approach, and its cut is not in line with the new flow angle produced by the main body pressure field.

For GlennICE and FENSAP-ICE the maximum thickness is not reached in a single shot approach. This could be due to needing a multi-shot approach or the computational ice density needs to decrease below 917 kg/m^3 even though this is a fully rime case. In addition, a pointed ice shape for the experiment is interesting for this rime condition. More investigation is needed by looking at the repeat rime icing runs to narrow down the causes for the point in the ice shape, but it could be due to the thin strut geometry.

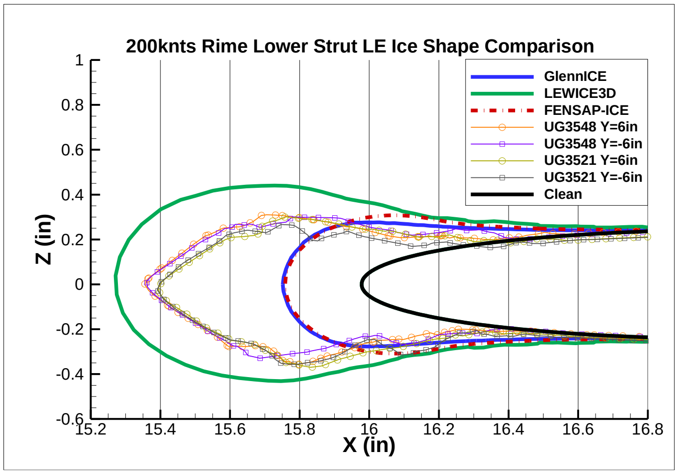

Figure 39. Computational ice shape vs. experimental UG3548 and UG3521 200 knots run on the strut LE at Y= 6 in slice for a 7 min icing duration.

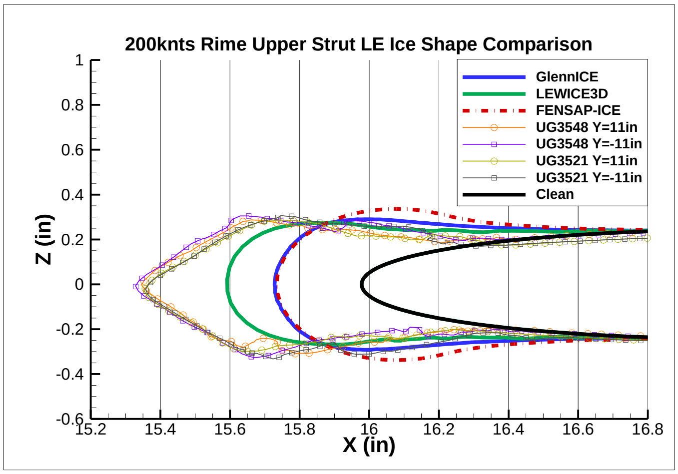

Figure 40. Computational ice shape vs. experimental UG3548 and UG3521 200 knots 0° AoA run on the strut LE at Y= 11 in slice for a 7 min icing duration.

Ice Accretion Analysis at 0° AoA and 150 knots

Ice shape comparisons for UG3538 150 knots can be seen in Figs. 41-44 with the icing codes matching the experimental better than the UG3538 200 knots case. In addition, Figs. 41-44 show what happens when changing $\rho_{ice} = 917\,kg/m^3$ (shown solid line) to $\rho_{ice} = 450\,kg/m^3$. GlennICE and FENSAP-ICE results were laying on top of each other for these plots with almost no deviation, so the FENSAP-ICE simulations were hidden to make the plots easier to read for this 150 knots case. Figure 41 shows changing the ice density to 450 kg/m^3 at the nose prediction increases the maximum ice thickness. LEWICE3D at $\rho_{ice} = 917\,kg/m^3$ gets the best match, but still shows a divot.

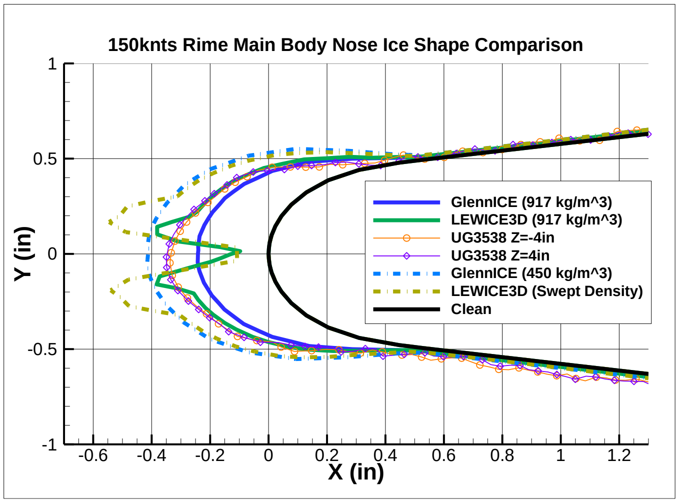

Figure 41. Computational ice shape vs. experimental UG3538 150 knots 0° AoA run at the main body nose for a 5 min icing duration.

Figure 42 shows how decreasing the ice density (GlennICE) or using the swept density model (LEWICE3D) puts the icing code slope ice thickness over the experimental ice laser scan result.

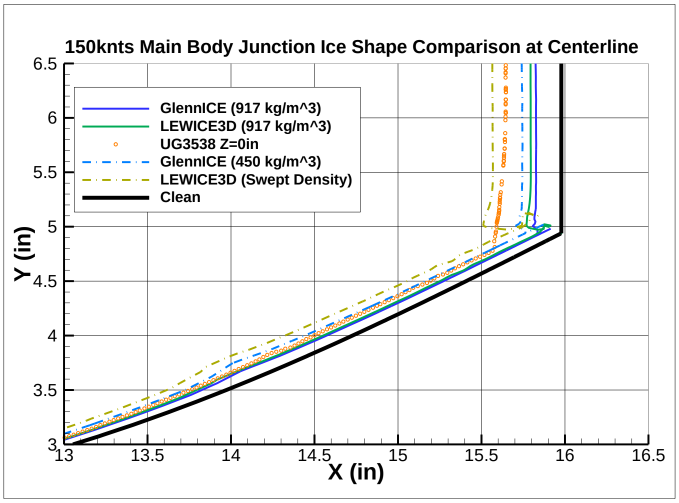

Figure 42. Computational ice shapes vs. experimental UG3538 150 knots 0° AoA run at the main body slope and strut junction for a 5 min icing duration.

Figures 43-44 show that the LEWICE3D at $\rho_{ice} = 917\,kg/m^3$ matches the experimental maximum ice thickness better, but the icing duration is shorter for this 150 knots case. When switching to $\rho_{ice} = 450\,kg/m^3$, a large ice shape is predicted by LEWICE3D for the lower strut cut (Y = 6 in). This seems to be due to a correction factor inside LEWICE3D at this swept flow location. Switching GlennICE to $\rho_{ice} = 450\,kg/m^3$ improves the computational prediction to the maximum ice thickness, but it still does not reach the max thickness. More investigation in the future will focus on the experimental ice weights to narrow down the ice density on this thin strut.

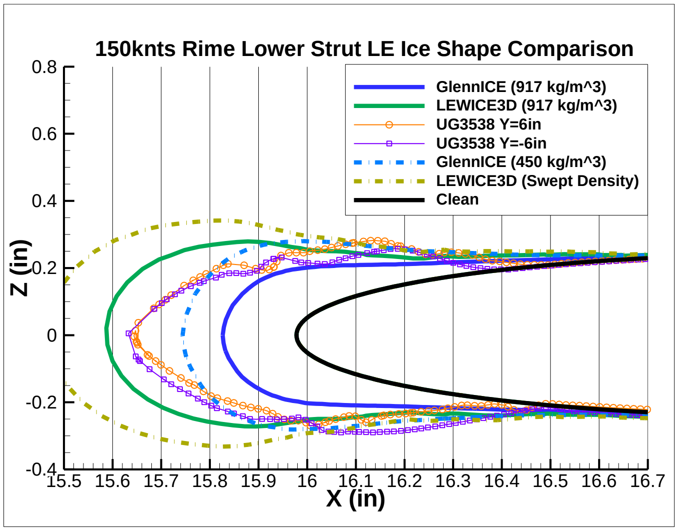

Figure 43. Computational ice shape vs. experimental UG3538 150 knots 0° AoA run on the strut LE at Y= 6 in slice for a 5 min icing duration.

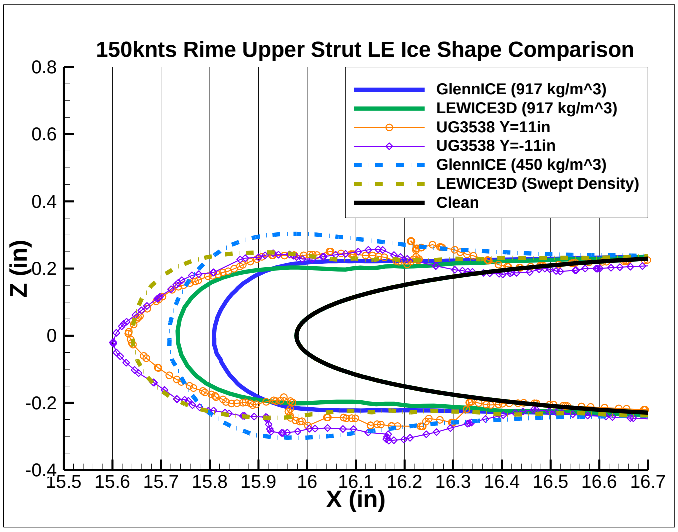

Figure 44. Computational ice shape vs. experimental UG3538 150 knots 0° AoA run on the strut LE at Y= 11 in slice for a 5 min icing duration.

Experimental Collection Efficiency Analysis for 4° AoA

The UG3540 150 knots 4° AoA rime case is interesting to see the effect of collection efficiency with angle of attack. At an angle of attack the pressure side can increase in total water catch. The LWC contour for this case is shown in Fig. 45, where the pressure side is increasing in LWC above freestream ($LWC = 0.45\ g/m^3$) and the suction side sees a large shadow zone (shown blue) coming off the nose. Above the shadow zone is a high concentration zone that strikes near the lower strut root on the non-instrumented strut.

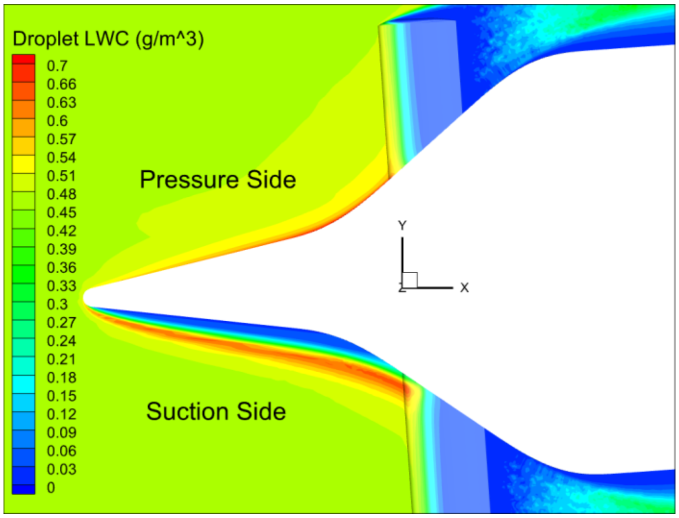

Figure 45. LWC contour at 150 knots at 4° AoA for composite to see high concentration zones.

Like before, a constant freestream method was explored for Eq. 3 on the main body and is shown in Fig. 46. A constant freestream tunnel velocity (77.1 m/s for this UG3540 case) and constant freestream tunnel LWC (0.45 g/m^3 for this case) were used. All three icing codes match each other well on the pressure side and the nose section where beta max is located. However, on the suction side three distinct spikes from the Lagrangian codes (GlennICE and LEWICE3D) are shown. These spikes correspond to the bin runs, so the three spikes are due to three different bins or droplet sizes striking those distinct locations further down the chord. Fig. 46 shows the results for back calculating experimental collection efficiency. In the $\rho_{ice} = 917\,kg/m^3$ curve (shown purple), the main body leading edge collection efficiency is captured well (where beta max is), but the slope collection efficiency is not captured well when comparing to computational predictions. Changing to the $\rho_{ice} = 450\,kg/m^3$ curve (shown orange) improves the pressure side match to experimental very well, but the beta max is significantly reduced. This might show that ice density is not constant at every chord location and the slope ice density might be between the two bounds used for constant ice density.

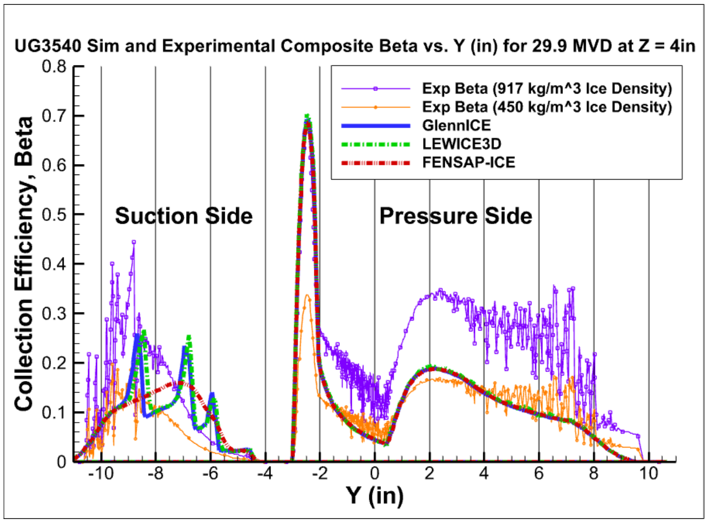

Figure 46. Simulation and experimental beta at the main body slice (Z = 4in) for UG3540 150 knots rime run.

The dry air velocity contour for this case is shown in Fig. 47 and shows the swept flow change between the instrumented strut on the pressure side and non-instrumented strut on the suction side. In general, the velocity near the strut leading edge is higher on the non-instrumented strut. This higher velocity increases the collection efficiency on the non-instrumented strut compared to the instrumented strut of interest.

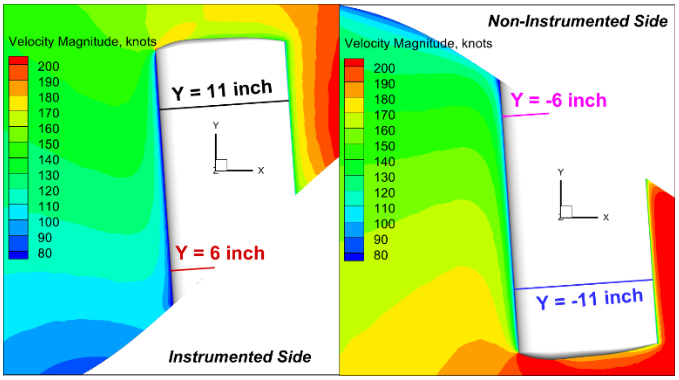

Figure 47. Dry air velocity flow field for UG3540 150 knots at 4° AoA.

The result in collection efficiency changes between both struts can be seen in Figs. 48-49 on the lower root strut slices (Y = 6 in and Y = -6 in). Beta max increases on the non-instrumented strut leading edge in Fig. 49 almost to 1. The experimental beta curve using $\rho_{ice} = 917\,kg/m^3$(shown red) also gets a better prediction to the icing codes results.

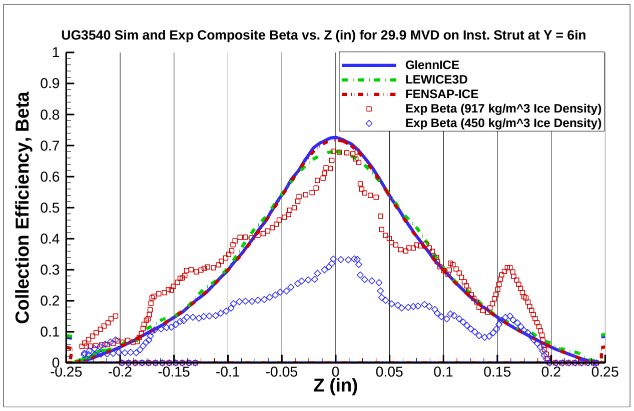

Figure 48. Simulation and experimental beta at the instrumented strut slice Y=6in for UG3540 150 knots at 4° AoA rime run.

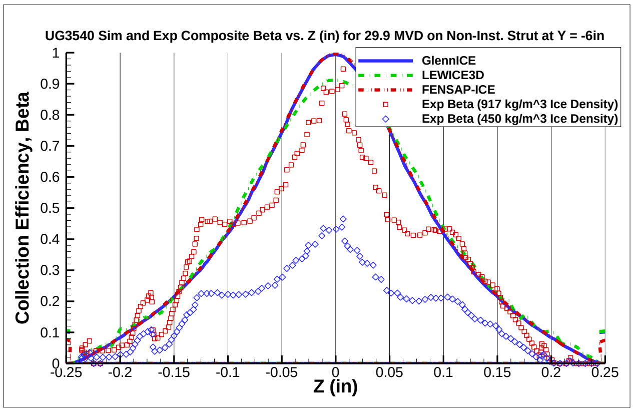

Figure 49. Simulation and experimental beta at the non-instrumented strut slice Y= -6in for UG3540 150 knots at 4° AoA rime run.

Figures 50-51 show the upper outboard strut slices (Y = 11 in and Y = -11 in) have a similar beta max now between the pressure side strut and the suction side strut leading edge. The experimental beta curve using $\rho_{ice} = 917\, kg/m^3$(shown red) matches the icing code better than the $\rho_{ice} = 450\, kg/m^3$(shown blue) curve, but the match is worse than at the lower root slice cuts shown in Figs. 48-49.

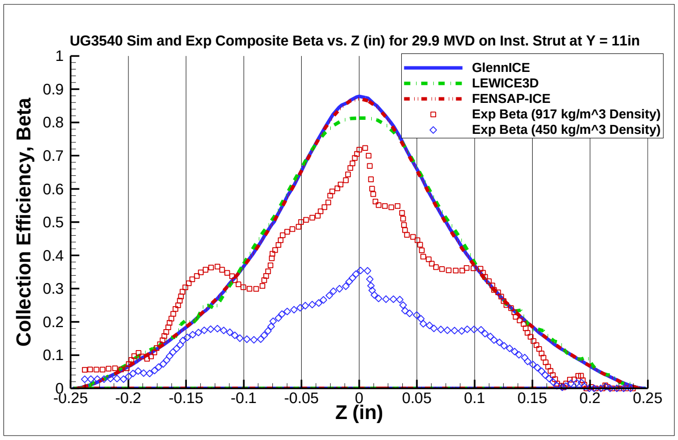

Figure 50. Simulation and experimental beta at the instrumented strut slice Y=11in for UG3540 150 knots at 4° AoA rime run.

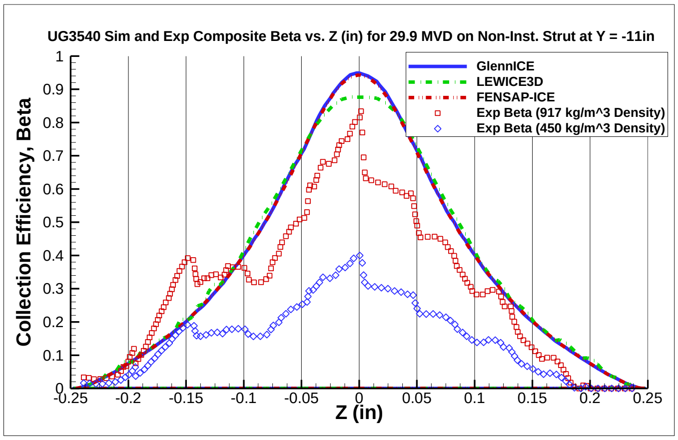

Figure 51. Simulation and experimental beta at the non-instrumented strut slice Y= -11in for UG3540 150 knots at 4° AoA rime run.

Ice Accretion Analysis at 4° AoA and 150 knots

Results for a single-shot approach and ice density held constant to $\rho_{ice} = 917\, kg/m^3$ results are shown in Fig. 52. All the data for the 4° AoA ice shapes and clean geometry has been rotated in x, y, and z coordinates so that the clean geometry is displaying at the 0° AoA position. GlennICE and FENSAP-ICE did not reach the maximum thickness (angled towards the pressure side) of the experimental rime ice shape at the main body "nose" or leading edge. LEWICE3D reached the maximum thickness without creating a divot like it did in the 0° AoA cases.

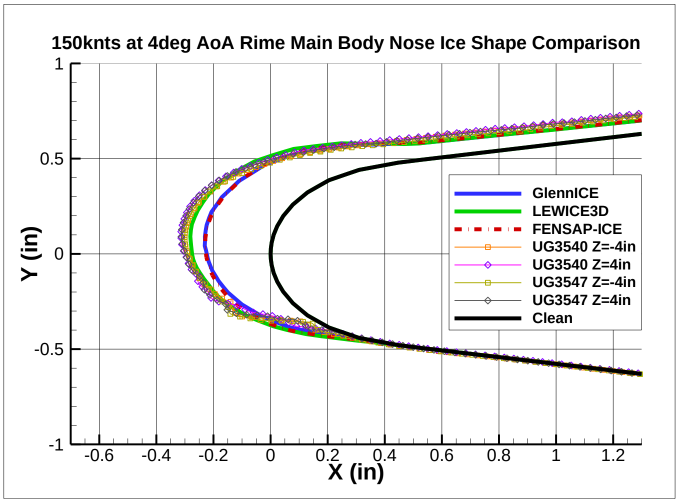

Figure 52. Computational ice shape vs. experimental UG3540 150 knots at 4° AoA run at the main body leading edge for a 5 min icing duration.

Figure 53 shows the icing code to experiment comparison at the instrumented strut "pressure side" and slope junction at the centerline (Z = 0). While Fig. 54 shows the comparison at the non-instrumented strut "suction side" and slope junction. More experimental ice thickness is on the pressure side slope, Fig. 53, compared to the suction side slope, Fig. 54. This is due to the increase in collection efficiency due to the angle of attack change. However, more ice exists on the non-instrumented strut leading edge in Fig. 54 due to the high LWC above the shadow zone impacting on the lower non-instrumented strut. The ice bumps on the root of the strut from GlennICE and FENSAP-ICE are artifacts from using limited discrete droplet distribution bins.

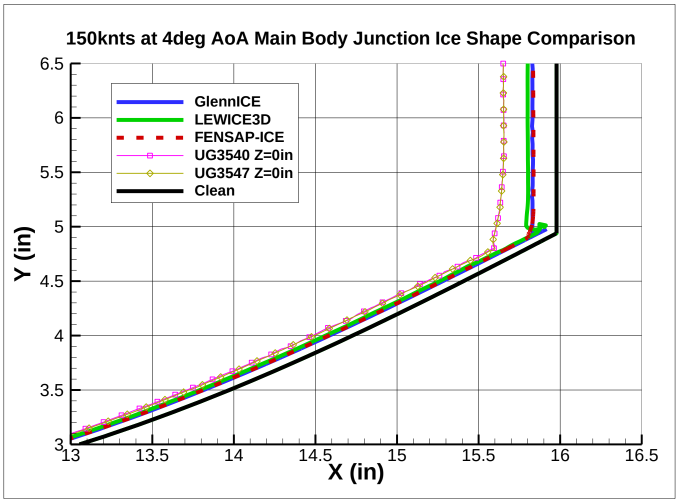

Figure 53. Computational ice shapes vs. experimental UG3540 150 knots at 4° AoA run at the main body slope and strut junction on instrumented side for a 5 min icing duration.

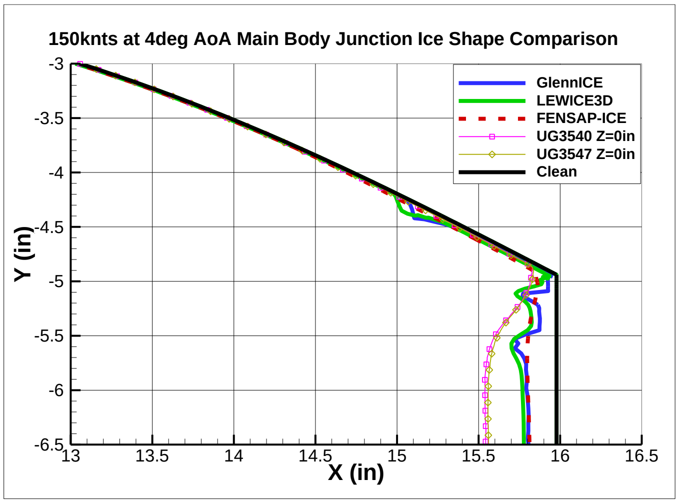

Figure 54. Computational ice shapes vs. experimental UG3540 150 knots at 4° AoA run at the main body slope and strut junction on non-instrumented side for a 5 min icing duration.

Ice comparisons on the instrumented strut lower root slice (Y = 6 in) can be seen in Fig. 55, and ice comparisons on the non-instrumented strut lower slice (Y = -6 in) can be seen in Fig. 56. LEWICE3D got closer in prediction than GlennICE and FENSAP-ICE to the experimental ice shapes on the instrumented strut in Fig. 55. LEWICE3D overpredicts the max ice thickness on Fig. 56 on the suction side.

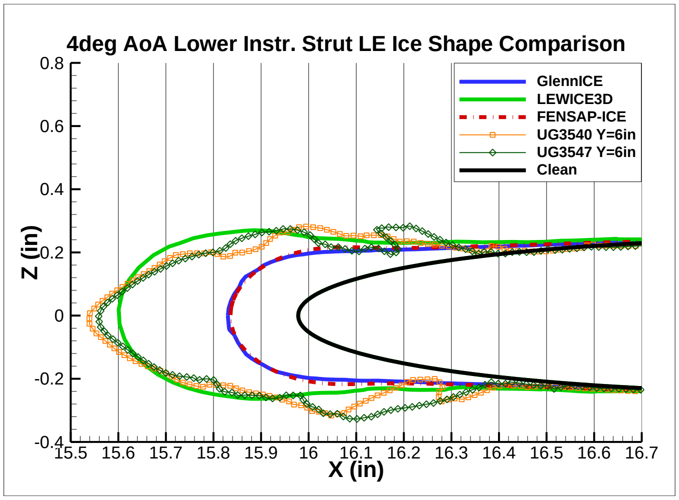

Figure 55. Computational ice shape vs. experimental UG3540 150 knots at 4° AoA run on the instrumented strut LE at Y= 6 in slice for a 5 min icing duration.

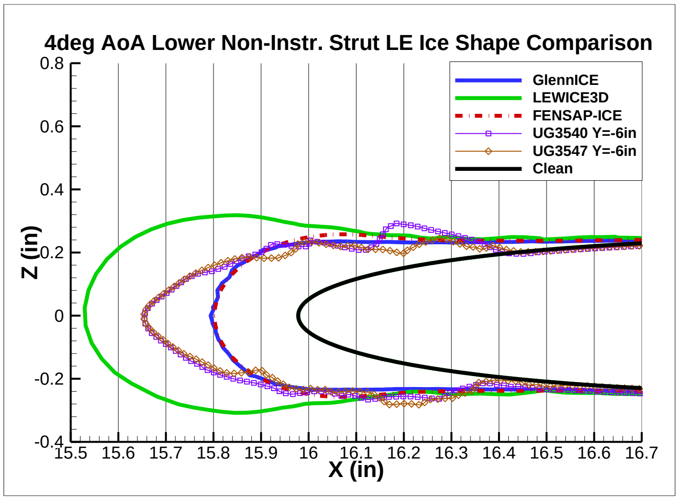

Figure 56. Computational ice shape vs. experimental UG3540 150 knots at 4° AoA run on the non-instrumented strut LE at Y= -6 in slice for a 5 min icing duration.

Ice comparisons on the instrumented strut upper outboard slice (Y = 11 in) can be seen in Fig. 57, and ice comparisons on the non-instrumented strut lower slice (Y = -11 in) can be seen in Fig. 58. Here the icing codes match the experimental ice shape better, but none of the three meet the maximum ice thickness. This might be due to using a single shot approach and using a constant ice density.

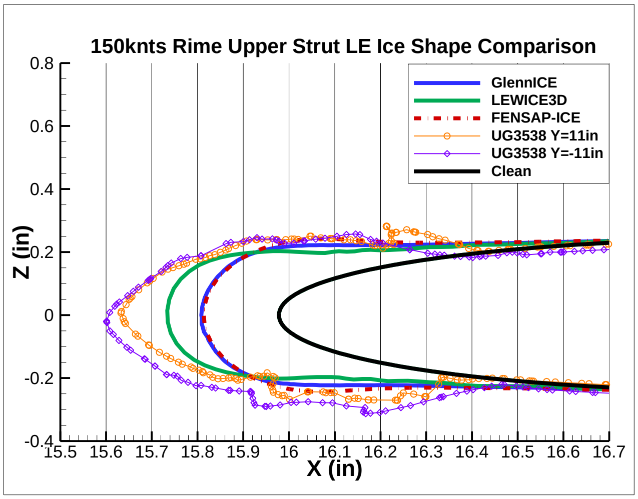

Figure 57. Computational ice shape vs. experimental UG3540 150 knots at 4° AoA run on the instrumented strut LE at Y= 11 in slice for a 5 min icing duration.

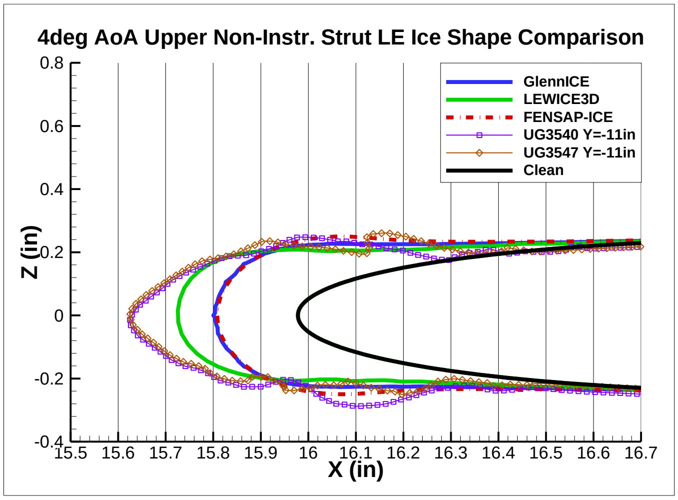

Figure 58. Computational ice shape vs. experimental UG3540 150 knots at 4° AoA run on the non-instrumented strut LE at Y= -11 in slice for a 5 min icing duration.

Conclusion

Computational aerothermal dry air and icing simulations were conducted on the SIDRM test article and compared to the experimental measurements collected from tests performed at the NASA IRT icing wind tunnel in early 2022. This paper covered an icing study analyzing different icing codes involving FENSAP-ICE (Eulerian approach), LEWICE 3D (Lagrangian approach), and GlennICE (Lagrangian approach) on SIDRM's complex body flow-field and results were compared to experimental aerothermal results and rime icing tunnel run data. Rime icing runs were chosen due to the objective of calculating collection efficiency through an empirical equation from the laser ice shapes. In addition, single-shot approaches in the icing codes do better in capturing rime ice shapes compared to glaze due to glaze icing having runback icing and a varying ice density as the ice grows.

Thermocouple and pressure taps results measured on the test article were compared to the computational dry air CFD simulations for surface pressure and temperature validation of the simulations before the icing cloud was turned on. The experimental to CFD results were in good agreement at the different tunnel airspeeds, and between the 0° and 4° angle of attack cases. The aerothermal thermocouple comparisons were closer in matching experimental than the 30 second dry air results before the rime icing cloud hit the test article. This might be because the test article's skin temperature does not reach full thermal equilibrium between the rime tunnel runs. Future analysis will focus on the thermocouples and the heat flux measurements to simulations, and that might narrow down this thermal equilibrium issue.

The ice shape at SIDRM's leading edge nose is captured using all three icing codes when using a constant ice density of $\rho_{ice} = 917\,kg/m^3$, but this area could benefit more with switching from a single-shot to multi-shot approach in the icing setup. The experimental beta calculation matches the predicted droplet code collection efficiency results at the nose (beta max) when assuming $\rho_{ice} = 917\,kg/m^3$ in Eq. 3.

Changing the constant ice density to $\rho_{ice} = 450\,kg/m^3$, improves the experimental beta calculation match on the main body slope to the droplet composite (7-bin) predictions from the three icing codes. To reduce the ice feathers complication, it is suggested to use shorter spray time runs to calculate collection efficiency from a rime 3D laser scan ice shape. However, for the ice shape comparisons, the computational single-shot ice shape overpredicts when changing $\rho_{ice} = 450\,kg/m^3$ on GlennICE compared to the experimental laser scan ice thickness. This suggests LWC, flow angle, droplet impact angle, or airspeed changes have more of an effect on the main body slope ice. Alternately, this may suggest that a single-shot approach is not as accurate for this sloped geometry ice accretion. The main body nose ice shape could have a greater effect on droplet trajectories impacting the ramp slope. Improvements on gathering experimental ice mass measurements in just this slope area are being implemented.

For the strut leading edge, GlennICE and FENSAP-ICE consistently underpredicted the ice shape no matter the chosen density. This strut leading edge area would benefit from a multi-shot approach comparison at the same constant ice densities. LEWICE3D matched the experimental lower strut slice (Y = 6 in) ice shape better when assuming $\rho_{ice} = 917\,kg/m^3$on the 0° cases, and $\rho_{ice} = 917\,kg/m^3$ on the instrumented strut "pressure side" on the 4° case. LEWICE3D's swept wing ice density model gave mixed results on the strut leading edge as well on the 150 knots and 0° case.

The test article angle of attack impacted the location of ice accretion on the main body slope and strut leading edges due to high LWC concentrations and airspeed flow changes. FENSAP-ICE and GlennICE single-shot results on the strut slices were identical, but underpredicted the maximum ice thickness. Changing the ice density $\rho_{ice} = 450\,kg/m^3$ improves the FENSAP-ICE and GlennICE prediction, but they still underpredicted the maximum thickness. A multi-shot approach might have better matching to the strut ice profile shapes. Utilizing the two constant ice densities bounded the results for much of the analysis, and more focus in future tests will be to measure the experimental ice density on separate locations of this test article.

References

1. Mason, J. G., Strapp, J. W., and Chow, P., "The Ice Particle Threat to Engines in Flight," *44th AIAA Aerospace Sciences Meeting and Exhibit*, AIAA, Reno, NV, 2006, AIAA-2006-206 https://doi.org/10.2514/6.2006-206.
2. Struk, P. M., Bartkus, T. P., Bencic, T. J., King, M. C., Ratvasky, T. P., Van Zante, J. F., and Tsao, J. C., "An initial

study of the fundamentals of ice crystal icing physics in the NASA propulsion systems laboratory," 9th AIAA Atmospheric and Space Environments Conference, June, 2017, pp. 1–40. https://doi.org/10.2514/6.2017-4242.

3. Struk, P. M., Agui, J., Ratvasky, T., King, M., Bartkus, T., and Tsao, J. C., "Ice-Crystal Icing Accretion Studies at the NASA Propulsion Systems Laboratory," SAE Technical Papers, Vol. 2019-June, No. June 2019, pp. 1–12. https://doi.org/10.4271/2019-01-1921.
4. Bartkus, T. P., Tsao, J. C., and Struk, P. M., "Analysis of Experimental Ice Accretion Data and Assessment of a Thermodynamic Model during Ice Crystal Icing," SAE Technical Papers, Vol. 2019-June, No. June 2019. https://doi.org/10.4271/2019-01-2016.
5. Bartkus, T. P., Lee, S., Potapczuk, M. G., and Flack. C. A., "Description of Cloud Characterization and Icing Tests for a 3D Heated Test Article at the NASA Icing Research Tunnel," *AIAA AVIATION 2022 FORUM*, AIAA, Chicago, IL, 2022, AIAA-2022-3700 https://doi.org/10.2514/6.2022-3700.
6. Bartkus, T., Potapczuk, M., Lee, S., Stewart, E., and Chen, R.-C., "Plans for Ice Crystal Icing Tests Using a 3D Heated Test Article at the NASA Icing Research Tunnel," *AIAA AVIATION 2021 FORUM*, AIAA, Virtual Event, 2021, Oral Presentation.
7. William, Mathias. "General Electric GE90-94B Turbofan Engine". https://grabcad.com/library/general-electric-ge90-94b-turbofan-engine-1. GrabCAD. Nov. 2016.
8. SAE Aerospace. *Aircraft Inflight Icing Terminology*. SAE International, April 2013. ARP5624. https://doi.org/10.4721/ARP5624.
9. "ANSYS FENSAP-ICE User Manual," Release 2021 R1, ANSYS, Inc., 2021.
10. Bidwell, C.S., and Potapczuk, M.G., "User's Manual for the NASA Lewis Three-Dimensional Ice Accretion Code (LEWICE3D)," NASA/TM 105974, 1993. https://ntrs.nasa.gov/citations/19940017117.
11. "GlennICE User Manual Software Version 2.2.0", NASA, June 2022.
12. Bartkus, T. P. and Stewart. E. A., "Icing Physics Studies using the 3D SIDRM Test Article: Aerodynamic and Supercooled Liquid Icing Analysis," *SAE International Conference on Icing of Aircraft, Engines, and Structures*, SAE, Vienna, Austria, 2023 (submitted for consideration).
13. "ANSYS Fluent Theory Guide," Release 2021 R1, ANSYS, Inc., 2021.
14. Bourgault, Y., Beaugendre, H., and Habashi, W.G., "Development of a Shallow Water Icing Model in FENSAP-ICE", *AIAA Journal of Aircraft*, Vol. 37, No. 4, 2000, pp. 640-646. https://doi.org/10.2514/2.2646.
15. Bidwell, Colin. "Icing Analysis of the NASA S3 Icing Research Aircraft Using LEWICE3D Version 2." *SAE Technical Paper Series*, 2007, https://doi.org/10.4271/2007-01-3324.
16. Wright, W., Porter, C., Galloway, E., and Rigby, D. "An Automated Refinement Process for Particle Trajectory Methods in GlennICE," AIAA AVIATION 2021 FORUM, AIAA, Virtual Event, 2021, https://doi.org/10.2514/6.2021-2631.
17. Porter, C. E., "A Comparison of Trajectory Refinement Schemes for GlennICE," *AIAA AVIATION 2022 FORUM*, AIAA, Chicago, IL, 2022, https://doi.org/10.2514/6.2022-3692.
18. Timko, Emily N, et al. NASA Glenn Icing Research Tunnel: 2019 Cloud Calibration Procedure and Results NASA/TM-20205009045, 2021 https://ntrs.nasa.gov/citations/20205009045.
19. Anderson, D. and Tsao, J. Overview of Icing Physics Relevant to Scaling NASA CR 2008-213851, 2008. https://ntrs.nasa.gov/citations/20050215167.
20. Tsao, Jen-Ching and Lee, Sam. Evaluation of Icing Scaling on Swept NACA 0012 Airfoil Models NASA/CR-2012-217419, 2012 https://ntrs.nasa.gov/citations/20120009186.
21. Tsao, Jen-Ching, and Christopher E. Porter. "Characterization of Collection Efficiency of the Common Research Model Midspan Wing Section in the IRT." AIAA AVIATION 2021 FORUM, 28 Aug. 2021, https://doi.org/10.2514/6.2021-2681.

Contact Information

Eric Stewart
Work phone: (210) 833-4647
E-mail: eric.a.stewart@nasa.gov
Affiliation: Naval Air Warfare Center Aircraft Division (NAWCAD)